Ceramics International 52 (2026) 38807–38821

Contents lists available at ScienceDirect

Ceramics International

journal homepage: www.elsevier.com/locate/ceramint

Magnetically responsive ferrite/organoclay composites for water remediation

Giulia Rando [a,1], Tatiana Rodriguez-Flores [b,1], Silvia Sfameni [a], Falak Shafiq [b], Matteo Cantoni [c], Maria Rosaria Plutino [a,*,2], Roberto Nisticò [b,**,2]

[a] Institute for the Study of Nanostructured Materials (ISMN–CNR), URT Messina, c/o Department of ChiBioFarAm, University of Messina, Viale F. Stagno d'Alcontres 31, Messina, 98166, Italy
[b] University of Milano-Bicocca, Department of Materials Science, U5, INSTM, Via R. Cozzi 55, Milano, 20125, Italy
[c] Politecnico di Milano, Department of Physics, Via G. Colombo 81, Milano, 20133, Italy

ARTICLE INFO

Keywords:
Adsorption
Clays
Environmental remediation
Ferrites
Magnetic materials

ABSTRACT

Magnetic ferrite/organoclay composites were developed as magnetically recoverable adsorbents for water remediation. Spinel ferrites (*i.e.*, $CoFe_2O_4$ and $NiFe_2O_4$) were incorporated into an organically modified montmorillonite clay using GPTMS and APTES alkoxysilanes as coupling agents. These composite materials, along with pristine ferrites and montmorillonite, were characterized in terms of morphology, structure, surface properties, and magnetic behavior. Magnetic ferrite/organoclay composites were tested as sorbing substrates for the removal of Methylene Blue dye species from aqueous matrix. Compared to pristine ferrites (3.58–2.93 mg g^{-1}), the composites exhibited enhanced adsorption capacities of 4.73 mg g^{-1} ($CoFe_2O_4$-based composite, with removal efficiency of 50.6%) and 8.29 mg g^{-1} ($NiFe_2O_4$-based composite, with removal efficiency of 88.5%). Kinetic analysis indicated the predominance of pseudo-second-order mechanisms, suggesting the involvement of surface-mediated interactions. Magnetic composites exhibited enhanced adsorption performances compared to pristine ferrites, with maximum capacities of 8.46 mg g^{-1} ($CoFe_2O_4$-based composite) and 13.44 mg g^{-1} ($NiFe_2O_4$-based composite), and distinct adsorption behaviors described by Langmuir (monolayer coverage) and Temkin (more governed by adsorbent–adsorbate interactions and adsorption energy) models, respectively. The efficacy, structural integrity, and facile magnetic separation of these sorbent systems demonstrate significant potential as stable, recoverable materials for sustainable water remediation.

1. Introduction

Nowadays, the anthropogenic impact caused by extensive industrialization concentrated in a few economic areas (with different environmental laws) combined with the rapid growth of the global population with their relative nutritional and energy demands, has already become a serious concern to the health of global environment. Addressing it requires rapid and proficient technological solutions. Environmental pollution is among the main causes affecting the availability of clean water sources, thus dramatically limiting the direct access to safe and clean water in many areas of the globe [1,2]. Hence, to provide widespread and consistent access to clean water, several (waste) water treatment plants have been established, especially near overpopulated urban areas, to properly remediate contaminated water effluents into drinkable water [3,4]. In particular, common (waste)water treatment facilities utilize a combination of various mechanical/-physical, chemical, and (an)aerobic biological processes to effectively remove contaminants from domestic and industrial effluents, thus enabling their reuse either as potable water or in agricultural and industrial applications [5]. Although conventional (waste)water treatment technologies are well-consolidated, the recent rise of a new class of microcontaminants defined as "emerging pollutants" (which are a wide group of chemicals not covered by existing water-quality regulations, *e.g.*, pharmaceuticals, drugs, additives, dyes, etc.) has become a growing

* Corresponding author.
** Corresponding author.
E-mail addresses: mariarosaria.plutino@cnr.it (M.R. Plutino), roberto.nistico@unimib.it (R. Nisticò).
[1] Both authors contributed equally to this work.
[2] Both authors contributed equally to this work as senior authors.

https://doi.org/10.1016/j.ceramint.2026.06.336
Received 8 March 2026; Received in revised form 12 June 2026; Accepted 22 June 2026
Available online 23 June 2026

concern, as conventional treatment processes are often unable to remove them efficiently [6–8]. For effective removal of such emerging pollutants from contaminated effluents, innovative advanced treatments (*e.g.*, homogenous/heterogeneous photocatalytic processes) are required [9,10]. Despite the evidence that these advanced treatments are promising technologies at the laboratory scale, in most cases, these processes are poorly applicable at the industrial scale and/or weakly integrable into traditional (waste)water treatment plants, thus limiting their effective utilization [11,12].

As reported in the literature, adsorption is a surface phenomenon involving the adherence of chemical species (*adsorbates*) at the surface of a solid (*adsorbent*) through physical or chemical interactions. Conventional adsorbents often used in common (waste)water treatment plants include highly porous activated carbons, clays, and resins [13–15]. However, even if these sorbing systems are quite efficient, their recovery from the decontaminated aqueous medium requires either further separation/filtration processes, or an immobilization step, followed by an additional regeneration phase [16].

In recent years, magnetic nanomaterials have gained increasing consideration in (waste)water remediation due to their cost-effectiveness and ease of recovery through the application of an external magnetic field, enabling them as a compelling alternative to conventional sorption systems [17,18]. In particular, the most investigated magnetic nanomaterials are magnetite (Fe_3O_4) and maghemite (γ-Fe_2O_3) crystal phases, which are two ferrimagnetic materials (or eventually superparamagnetic systems depending on the particles' size), mainly due to their environmental friendliness, natural abundance, low cost, and relatively high magnetic responsiveness [19–21]. Other magnetic systems potentially exploitable for their improved magnetism include zero-valent metallic nanoparticles (*e.g.*, ZVI, which is a ferromagnetic system) [22] and ferrite-based systems (*i.e.*, a class of mixed oxide compounds with enhanced magnetic response due to the co-presence of other elements such as Co and Ni with Fe) [23,24].

Hence, magnetic hybrid/composite systems, with a magnetic core covered by a functional (in)organic shell (whose action is to provide a specific sorption ability), constitute an advanced strategy for designing recoverable adsorbents for (waste)water remediation [25]. Regarding the functional (in)organic shells, the literature reports numerous case studies evidencing the possibility of covering or grafting the surface of magnetic nanoparticles with functional (in)organic shells, which serve as sorption sites for the selective removal of microcontaminants from aqueous media [26–28].

In this regard, clay-based composite materials represent an attractive class of functional systems for environmental applications due to their natural abundance, low environmental impact, and intrinsic structural versatility, possessing properties like high surface area, ion exchange, and controlled release, making them ideal for water purification, soil remediation, sustainable building, and even energy storage [29]. The combination of inorganic clay matrices with functional molecules, nanofillers, and organic or hybrid networks enables the development of multifunctional materials with tailored surface chemistry, enhanced stability, and improved performance [30]. Moreover, sol–gel chemistry has emerged as an effective strategy to act as a cross-linking route, allowing the formation of robust organic–inorganic hybrid networks under mild and environmentally friendly conditions. The sol–gel process promotes strong interfacial interactions between the clay surface and functional organic/inorganic moieties, hence ensuring structural integrity, durability, and resistance to leaching [31]. Furthermore, sol-gel-derived hybrid clay composites can be designed for reusability and facile regeneration, hence supporting circular and sustainable material principles. These features make clay-based sol–gel-crosslinked composites highly promising as efficient, functional, and sustainable materials for advanced environmental remediation technologies [32,33].

Clays are one of the primary porous systems that can be exploited in environmental clean-up processes. They are naturally occurring 2D layered minerals extracted from the earth, composed of phyllosilicates and containing some minor impurities [34,35]. Clays can be classified into many subgroups according to their chemical composition and structural stacking. In particular, montmorillonite (*i.e.*, one of the most important and largely investigated clays) belongs to the smectite subgroups, which are characterized by a high ion exchange capacity due to the presence of both water molecules and many cations in the interlayer [34]. Furthermore, clays, particularly montmorillonite due to its structure, can be properly modified by introducing different organic moieties into the interlayer, thereby increasing the systems' hydrophobicity and consequently favoring the interaction between the sorption system and the target organic contaminants [36–39]. According to the literature, the possibility of integrating ad hoc functionalized clays with magnetic systems presents a very promising technological solution in environmental clean-up processes, especially for the capture of charged species by exploiting the clays' ion exchange ability. For instance, Yuan et al. [40] reported the synthesis of montmorillonite-supported magnetite nanoparticles following a co-precipitation method, and successfully tested them in the removal of Cr(VI) species from aqueous media, achieving a maximum adsorption capacity of *ca.* 15 mg g^{-1} primarily following the Langmuir model, whereas Jang et al. [41] reported the synthesis of magnetite nanoparticles supported on organically modified montmorillonite clay and tested them in the removal of iodine species, measuring a maximum adsorption capacity of *ca.* 322 mg g^{-1} according to the Langmuir model. Concerning ferrite-based systems, Haounati et al. [42] recently reported the incorporation of magnetic Co ferrite ($CoFe_2O_4$) nanoparticles into organically modified montmorillonite clay with sodium dodecyl sulfate and cetyltrimethylammonium bromide and successfully tested this system for the removal of Malachite Green dye, reaching the impressive maximum adsorption capacity of *ca.* 1245 mg g^{-1}, as per the Langmuir model. Interestingly, Mahmoud et al. [43] reported the synthesis of an activated nano-bentonite/$CoFe_2O_4$/carboxymethylcellulose composite and tested it against the abatement of Cr(VI) ions, demonstrating a preferential multilayer adsorption mechanism (Freundlich model) with a maximum adsorption capacity of *ca.* 45 mg g^{-1}. Lastly, Ahmadi et al. [44] reported the synthesis of a nanocomposite made by montmorillonite clays with starch and $CoFe_2O_4$. The uptake tests demonstrated a preferential multilayer adsorption mechanism against Methylene Blue (MB) and Methyl Violet dyes with maximum adsorption capacities of *ca.* 48 mg g^{-1} and 44 mg g^{-1}, respectively. In particular, this study deeply discussed all the possible mechanisms involved, evidencing the key role played by the substrate's porosity, electrostatic and surface interactions, hydrogen bonds, as well as π-π interactions between the aromatic rings of the target dyes and the starch structure.

On the other hand, the sol–gel approach represents a versatile and effective route for the surface modification of inorganic substrates and functional nanofillers, facilitating the development of hybrid organic–inorganic networks with controlled chemistry and high structural stability. In this context, alkoxysilanes are widely employed as coupling agents due to their bifunctional nature, which enables simultaneous participation in inorganic condensation reactions and organic functionalization processes. Upon hydrolysis of the trialkoxysilyl groups, silanol moieties are generated, which subsequently undergo condensation reactions to form stable Si–O–Si linkages, leading to the formation of a three-dimensional sol–gel-derived network. This process ensures strong anchoring of the hybrid matrix to mineral surfaces such as clays, while promoting cross-linking within the coating itself [45].

Among the commonly used organosilanes, (3-aminopropyl)triethoxysilane (APTES) and (3-glycidyloxypropyl)trimethoxysilane (GPTMS) serve complementary roles in the development of organically modified inorganic systems. APTES provides terminal amine groups that can interact with negatively charged clay surfaces and participate in further chemical reactions, while GPTMS contains an epoxy functionality capable of undergoing ring-opening reactions with nucleophilic groups, such as amines or surface hydroxyls. The concurrent presence of

APTES and GPTMS favors the formation of a chemically interconnected hybrid network in which organic functionalities are covalently linked to the inorganic backbone [46–48].

Hence, the present study focuses on the preparation of magnetic ferrite/organoclay composite systems and their testing as magnetic sorbing systems for the removal of Methylene Blue (MB) dye from aqueous matrix. In particular, two magnetic spinel ferrites were synthesized, namely Co ferrite ($CoFe_2O_4$) and Ni ferrite ($NiFe_2O_4$), through a co-precipitation method followed by an annealing treatment at 700 °C. Subsequently, montmorillonite clay was organically modified by employing a sol-gel method in the presence of the two selected alkoxysilanes GPTMS and APTES, to promote the effective integration and stabilization of magnetic spinel ferrites within the organoclay structure.

Unlike conventional organoclays modified through ion-exchange with surfactants (*e.g.*, CTAB or SDS), which may exhibit thermal and chemical instability, the synergistic use of APTES and GPTMS ensures the formation of a robust, cross-linked hybrid 3D-architecture. This approach not only stabilizes the magnetic ferrites within the clay layers, but also creates a stable functional hosting environment that prevents the leaching of the organic modifiers during the remediation process.

Pristine ferrites (*i.e.*, $CoFe_2O_4$ and $NiFe_2O_4$) and montmorillonite, along with organically modified montmorillonite, and the resulting nanocomposites (*i.e.*, $CoFe_2O_4$/modified-montmorillonite and $NiFe_2O_4$/modified-montmorillonite, respectively) were deeply physico-chemically, morphologically, structurally, and magnetically characterized by means of Fourier transform infrared spectroscopy in attenuated total reflection mode (ATR-FTIR), scanning electron microscopy (SEM), x-ray powder diffraction (XRPD), BET specific surface area analyses, and vibrating sample magnetometer (VSM), respectively. Furthermore, both pristine magnetic ferrites and the relative magnetic ferrite/organoclay composites were tested in environmental clean-up processes, investigating their performances against the abatement of MB dye solution. Given the real-world application of these substrates, both kinetics and adsorption isotherms were successfully evaluated, with the later accomplished through precise application of the Langmuir, Freundlich, and Temkin adsorption models, leading to the pertinent insights regarding the potential adsorption mechanism.

2. Experimental

2.1. Chemicals

Reactants: Iron(III) nitrate nonahydrate ($Fe(NO_3)_3 \bullet 9H_2O$, 98.0-101.0% CAS 7782-61-8, Thermo Scientific), cobalt(II) nitrate ($Co(NO_3)_2 \bullet 6H_2O$, 99%, CAS 10031-43-3, Alfa Aesar), nickel(II) nitrate hexahydrate ($Ni(NO_3)_2 \bullet 6H_2O$, 98%, CAS 13478-00-7, Alfa Aesar), sodium hydroxide pellets (NaOH, ACS reagent standards with purity ≥98%, CAS 1310-73-2, Sigma-Aldrich), montmorillonite K10 (CAS 1318-93-0, Sigma-Aldrich), (3-Glycidyloxypropyl)trimethoxysilane (hereafter GPTMS, purity ≥98%, CAS 2530-83-8, Sigma-Aldrich), (3-Aminopropyl)triethoxysilane (hereafter APTES, purity ≥98%, CAS 919-30-2, Sigma-Aldrich), and Methylene Blue dye (MB, CAS 122965-43-9, Sigma-Aldrich). Solutions and solvents: deionized water, hydrochloric acid (HCl, ACS reagent, purity 37%, CAS 7647-01-0, Sigma-Aldrich), ethanol (ACS reagent, purity ≥99.5%, CAS 64-17-5, Sigma-Aldrich), and acetone (CAS 67-64-1, Sigma-Aldrich) were used during washing procedures. Milli-Q water with a resistivity of 18.2 MΩ cm was used. All chemicals were used without further purification.

2.2. Synthesis of magnetic ferrite systems

The synthesis of magnetic ferrites (*i.e.*, $CoFe_2O_4$ and $NiFe_2O_4$) was carried out following a conventional co-precipitation method, as in De Pasquale et al. [49]. Initially, the desired amount of inorganic salts, both bivalent ions (either Co^{2+} or Ni^{2+}, 4.1 mmol), and Fe^{3+} (8.2 mmol) were dissolved in distilled water (75 mL), maintaining a fixed molar ratio of 1:2 (M:Fe), where M represents the bivalent Co/Ni ions. Subsequently, 5 M NaOH solution (15 mL) was added dropwise (delivery time: 10 min), maintaining the solution under constant stirring to better control the pH and ensure a homogeneous precipitation of the oxides. The reaction mixture was gradually heated up to 90 °C and maintained in isothermal conditions for 2 h under continuous stirring. Afterwards, the solid precipitate was recovered by centrifugation (6000 rpm, 10 min) and washed three times with deionized water and once with acetone to remove impurities. The resulting material was then oven-dried at 80 °C overnight. Finally, the dried solids were manually ground and calcined in a Carbolite CWF1200 muffle furnace (*Carbolite, Hope, UK*) with the following thermal program: (i) heating ramp from RT to 700 °C (heating rate: 10 °C·min^{-1}), (ii) isothermal step at 700 °C for 5 h, and (iii) cooling step from 700 °C to 50 °C (cooling rate: 5 °C·min^{-1}).

2.3. Synthesis of (magnetic) montmorillonite-based systems

For the preparation of (magnetic) montmorillonite-based systems (Fig. 1), montmorillonite was first organically modified (Fig. 1a) using a sol-gel method with selected alkoxysilanes. Specifically, 0.4 g of montmorillonite clay was gradually dispersed in 200 mL of ethanol in a round-bottom flask, and the mixture was stirred and heated at 70 °C for 1 h. Subsequently, GPTMS (3.5 g, 0.0148 mol), APTES (3.28 g, 0.0148 mol), and 2 mL of 0.1 M HCl (as a catalyst) were added dropwise in sequence. The reaction was allowed to proceed under stirring at 70 °C for 24 h. The resulting solid was recovered by centrifugation and subsequently dried at 60 °C for 2 days.

Next, the synthesized magnetic ferrite nanoparticles (200 mg) were dispersed and incorporated into an aqueous organoclay suspension (100 mg in 100 mL), resulting in a 2:1 mass ratio (ferrite:clay), using ultrasonic treatment for 2 h. The resulting precipitate was separated by centrifugation, rinsed several times with deionized water, and dried at 60 °C for 24 h. The final products, defined as $CoFe_2O_4$/modified-montmorillonite and $NiFe_2O_4$/modified-montmorillonite (Fig. 1b), were obtained as brown powders, and their structure and properties were subsequently characterized.

2.4. Characterizations

Fourier transform infrared spectra (ATR-FTIR) were collected directly on powder samples using a Jasco V-6600 spectrometer (JASCO Europe s.r.l., Cremella, LC, Italy) equipped with an Attenuated Total Reflection accessory. The instrument was operated with the Spectra Manager™ Suite, which includes the integrated KnowItAll® Informatics software and the JASCO Edition database (JASCO Europe s.r.l., Cremella, LC, Italy). Measurements were performed at room temperature (RT) over the 4000–400 cm^{-1} range, with each spectrum obtained from 32 scans at a resolution of 4 cm^{-1}.

Scanning electron microscopy (SEM) micrographs were obtained using a Zeiss Gemini 500 microscope equipped with a field emission source (FEG) and a Bruker Quantax detector for energy-dispersive X-ray spectroscopy (EDS) microanalysis. The microscope was operating at an acceleration voltage of 5.00 kV, and micrographs were captured using the "in-lens" detector. Samples were deposited onto SEM stubs using a double-adhesive carbon tape, then they were covered with an Au coating to prevent charging effects using a VPI SD-900C sputter coater.

X-ray powder diffraction (XRPD) analysis was carried out using a Rigaku Miniflex 600 diffractometer equipped with a copper radiation source operating at 40 kV and 15 mA. Diffraction data were collected across a 2θ range of 5-80°2θ, employing a fine step size of 0.02°. Pattern identification and lattice parameter determination were conducted using PDXL-2 software, referencing the ICDD database for phase matching. The average crystallite size (τ, nm), was determined using the Scherrer equation, considering the crystal reflection at 35.1 ± 0.2°2θ (corresponding to the Miller indexes (400) and (024)) in the case of

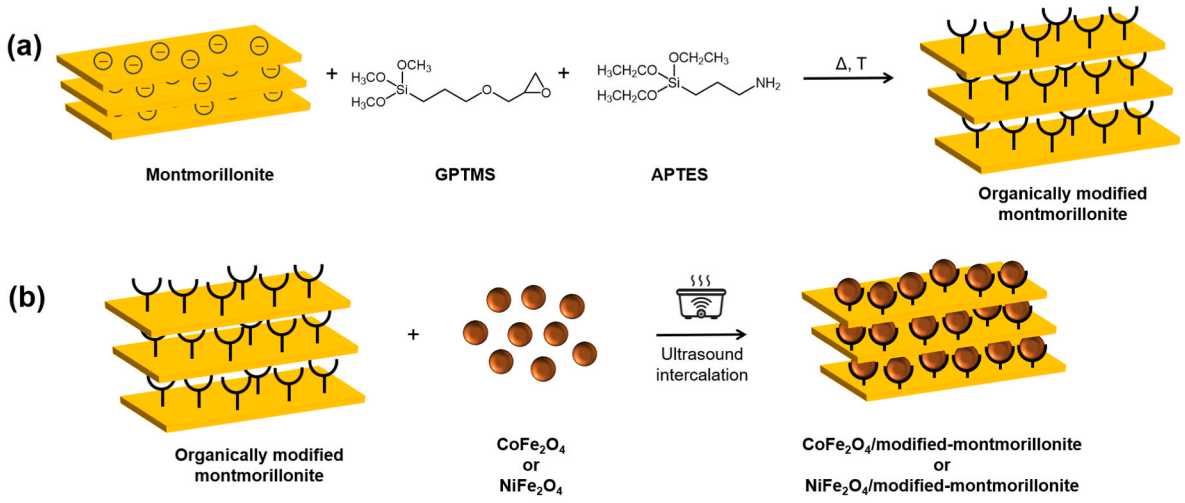

Fig. 1. Schematic illustration of the synthesis of organically modified montmorillonite (a) and magnetic montmorillonite-based composites (b) by means of sol-gel technique.

magnetic ferrite systems, whereas the crystal reflection at 8.8° 2θ (corresponding to the Miller indexes (001)) was considered in the case of montmorillonite clay.

Surface area analyses were performed using a Brunauer–Emmett–Teller (BET) method to determine the specific surface area. Measurements were carried out at 77 K using nitrogen as an adsorbate on an Autosorb iQ instrument equipped with ASiQwin software. Before analysis, samples were outgassed at 80 °C for 24 h.

Magnetic characterization of all magnetic samples was conducted at RT using an EZ-9 MicroSense Vibrating Sample Magnetometer (VSM), offering a sensitivity of 1 μemu and a maximum applied magnetic field of 2.25 T. Samples were housed in quartz cuvettes for measurement, and before data acquisition, all cuvettes were tested to ensure no ferromagnetic interference. To account for background signals, the intrinsic diamagnetic contribution of the quartz was evaluated using empty cuvettes and automatically subtracted from the sample data.

UV-Vis spectra were recorded using a Jasco V-770 UV-Vis spectrophotometer (JASCO Europe s.r.l., Cremella, LC, Italy) operating at *ca.* 25 °C. The instrument was equipped with standard measurement and analysis programs and utilized the Spectra Manager™ Suite spectroscopy software (JASCO Europe s.r.l., Cremella, Italy).

2.5. Testing

For the study of the adsorption properties of the ferrites, 10 mg of material was used and immersed in an MB solution at a concentration of 5 mg L^{-1} (total volume: 20 mL, pH = 7). At each time interval, the absorbance was measured using a UV-Vis spectrophotometer at λ = 664 nm and a temperature of 25 °C, employing a magnet to separate the magnetic systems during the sampling of the analyzed aliquot. The experiments were performed under limited light exposure.

Calibration curves and adsorption experiments for MB were performed using a Jasco V-770 UV-Vis spectrophotometer at *ca.* 25 °C. The concentrations of MB were measured at λ = 664 nm.

The removal efficiency (%) of MB dye by the different systems was calculated using the following Eq. (1):

$$\% = \frac{(C_0 - C_t)}{C_0} \times 100\% \quad (1)$$

where C_0 (expressed in mg·L^{-1}) is the initial dye concentration, and C_t (expressed in mg·L^{-1}) is the concentration at the target time.

The adsorption capacity (q_t, expressed as mg·g^{-1}) was calculated using the following Eq. (2):

$$q_t = \frac{(C_0 - C_t)V}{W} \quad (2)$$

C_0 and C_t (both expressed as mg·L^{-1}) are the initial and time-dependent dye concentrations, V (expressed in L) is the solution volume, and W (expressed in g) is the mass of the adsorbent.

2.6. Kinetics and isotherms modeling

Regarding the kinetic study, either $CoFe_2O_4$/modified-montmorillonite composite or $NiFe_2O_4$/modified-montmorillonite (10 mg) was utilized, in 5 mg L^{-1} MB solution (20 mL, pH = 7). After each time interval, the absorbance was measured using a UV–Vis spectrophotometer at λ = 664 nm and a temperature of 25 °C.

All the parameters were calculated from the graph of the adsorption capacity at time t (q_t; expressed in mg·g^{-1}) vs time (t; expressed in min). The coefficients of determination (R^2) for each of the tested models were examined and compared in order to establish which model provided the best fit to the experimental data.

For the pseudo-first-order calculation, the following Eq. (3) was employed [50,51]:

$$q_t = q_e\left(1 - e^{-k_1 t}\right) \quad (3)$$

t (expressed in min) is the contact time, q_t (expressed in mg·g^{-1}) is the adsorption capacity at time t, q_e (expressed in mg·g^{-1}) is the adsorption at equilibrium, and k_1 (expressed in min^{-1}) is the adsorption rate constant of the pseudo-first-order adsorption model.

For the pseudo-second-order calculation, the following Eq. (4) was employed [50]:

$$q_t = \frac{q_e^2 k_2 t}{1 + q_t k_2 t} \quad (4)$$

here t (expressed in min) is the contact time, q_t (expressed in mg·g^{-1}) is the adsorption capacity at time t, q_e (expressed in mg·g^{-1}) is the adsorption capacity at equilibrium, and k_2 (expressed in g·mg $^{-1}$ min^{-1}) is the adsorption rate constants of pseudo-second-order adsorption model.

Regarding the adsorption isothermal study, either $CoFe_2O_4$/modified-montmorillonite composite or $NiFe_2O_4$/modified-montmorillonite (10 mg) and 1, 2, 5, 10, and 15 mg L^{-1} MB solutions (20 mL) were employed. After a contact time of 24 h, the absorbance was measured using a UV–Vis spectrophotometer at λ = 664 nm and a temperature of 25 °C. All the parameters for the adsorption isotherm study were

calculated from the graph of the adsorption capacity at equilibrium (q_e; expressed in mg·g^{-1}) vs. the equilibrium dye concentration (C_e; expressed in mg·L^{-1}). The coefficients of determination (R^2) for each of the tested models were examined and compared in order to establish which model provided the best fit to the experimental data.

For the Langmuir calculation, the following Eq. (5) was employed [52,53]:

$$q_e = \frac{q_m k_L C_e}{1 + k_L C_e} \quad (5)$$

with C_e (expressed in mg·L^{-1}) representing the equilibrium dye concentration in the solution, k_L (expressed in L·mg^{-1}) is the Langmuir adsorption constant, and q_m (expressed in mg·g^{-1}) is the theoretical maximum adsorption capacity.

To better evaluate the Langmuir model's validity and the affinity between the MB dye and the composites, the dimensionless separation factor (R_L) was defined as follows:

$$R_L = \frac{1}{1 + K_L C_{max}} \quad (6)$$

K_L is the Langmuir constant and C_{max} is the highest initial dye concentration.

For the Freundlich calculation, the following Eq. (7) was used [52,54]:

$$q_e = k_F C_e^{1/n} \quad (7)$$

k_F (expressed in L·mg^{-1}) and n represent the Freundlich isotherm constants indicating the capacity and intensity of the adsorption, respectively.

For the Temkin calculation, the following Eq. (8) was employed [55–57]:

$$q_e = B_T \, ln(k_T C_e) \quad (8)$$

B_T (expressed in J·mol^{-1}) corresponds to RT/b (where T is the absolute temperature in K, and R is the universal gas constant) and k_T (expressed in L·mg^{-1}) is the Temkin isotherm constant related to the heat of adsorption.

3. Results and discussion

3.1. Characterization of bare magnetic ferrite systems

The ATR-FTIR spectra of $CoFe_2O_4$ and $NiFe_2O_4$ ferrites are shown in Fig. S1. Both materials exhibit the characteristic metal–oxygen stretching vibrations due to spinel ferrites in the low-frequency region. The absorption bands located at *ca.* 556 cm^{-1} are attributed to the stretching vibrations of Fe–O bonds in the tetrahedral sites [58]. These features confirm the successful formation of spinel-type structures. Besides, the broad band centered around 3500–3400 cm^{-1}, observed in the high-wavenumber region of both ferrites' spectra, corresponds to the stretching vibrations of surface-adsorbed hydroxyl groups (–OH) and/or physically adsorbed water molecules. The weak band at *ca.* 1640 cm^{-1} is attributed to the bending vibration of H–O–H, further supporting the presence of residual moisture on the particle surface, which is commonly observed in ferrite nanoparticles.

The distinct band at *ca.* 1441 cm^{-1} could be assigned to the stretching vibration modes of carbonate groups (CO_3^{2-}), probably originating from the adsorption of atmospheric CO_2 at the ferrite's surface [59]. The relative intensities and slight band shifts observed between $CoFe_2O_4$ and $NiFe_2O_4$ reflect differences in cation distribution and local bonding environments within the spinel lattice, consistent with the distinct nature of Co^{2+} and Ni^{2+} ions. Overall, the ATR-FTIR results confirm the spinel ferrite structure of both samples and highlight subtle compositional influences on the vibrational characteristics.

Morphological analysis of bare magnetic ferrite systems is reported in Fig. 2a and b. SEM micrographs reveal significant differences between the two magnetic ferrite systems. In the case of $CoFe_2O_4$ (Fig. 2a), a predominantly granular morphology is observed, revealing the presence of micrometric particles with rounded edges, along with aggregates of nanoscopic particles. In contrast, $NiFe_2O_4$ (Fig. 2b) exhibits an anisotropic rod-shaped morphology with average diameters of approx. 450 nm and lengths of several microns, with a relatively homogeneous distribution. Structural XRPD characterization is reported in Fig. 2c. The XRPD analysis performed on both ferrite samples confirms the presence of diffraction peaks attributable to spinel-type metal ferrites, with both $CoFe_2O_4$ and $NiFe_2O_4$ exhibiting similar diffraction patterns [60]. In the case of $CoFe_2O_4$, the XRPD pattern shows the main reflections at $2\theta = 30.1°$ (104), 35.4° (113), 37.0° (006), 43.1° (024), 53.4° (214), 56.9° (125), 62.5° (208), and 75.0° (226) belonging to the $CoFe_2O_4$ crystal phase (card number 01-079-1744) [61], whereas in the case of $NiFe_2O_4$, the XRPD pattern revealed the main reflections at $2\theta = 30.3°$ (220), 35.6° (311), 37.3° (222), 43.3° (400), 53.7° (422), 57.3° (511), 62.9° (440), 66.2° (531), 74.5° (533), confirming the presence of $NiFe_2O_4$ crystal phase (card number 01-080-0072) [62]. Furthermore, in the case of $CoFe_2O_4$ the presence of a large background signal at *ca.* 25° 2θ is attributable to the presence of a certain level of amorphous phase.

Table 1 reports the lattice parameters, the crystallite average sizes, the specific surface area (SSA), and magnetic properties for all magnetic ferrite systems. The average crystallite size is larger in the case of $CoFe_2O_4$ (*ca.* 18 nm) compared to $NiFe_2O_4$ (*ca.* 11 nm). Moreover, since both magnetic ferrite systems have a cubic unit cell, the lattice parameters are identical along all spatial directions (a = b = c), and similar in both samples (*i.e.*, 8.3 Å for both $CoFe_2O_4$ and $NiFe_2O_4$) [49].

In addition, N_2 adsorption–desorption isothermal profiles are reported in Fig. S3. Both curves exhibit a type IV profile, with a hysteresis loop of type H2 (from IUPAC classification) in the relative pressure range 0.4–1.0 for $NiFe_2O_4$, indicating a complex ink-bottle inter-particle mesoporosity, and of type H3 for $CoFe_2O_4$, indicating a slit-shape inter-particle mesoporosity. SSA values were calculated applying the BET equation, showing in both cases low SSA values, with $NiFe_2O_4$ exhibiting 22 m^2 g^{-1}, and $CoFe_2O_4$ exhibiting 16 m^2 g^{-1}. Magnetic properties of both magnetic ferrite systems, including magnetization saturation (M_s), coercivity (H_c), and remnant magnetization (M_r), are listed in Table 1, whereas magnetization curve profiles are reported in Fig. 2d (*i.e.*, an enlarged view of the central section of the hysteresis loop is reported in Fig. S2). Results indicated that both samples show a superparamagnetic behavior, with a hint of hysteresis (thus indicating a certain level of ferrimagnetism) in the case of $CoFe_2O_4$. As reported in Table 1, $CoFe_2O_4$ exhibits the highest M_s value (55.6 emu·g^{-1}) compared to $NiFe_2O_4$ (18.8 emu·g^{-1}). In contrast, $NiFe_2O_4$ showed a slightly higher H_c (17.4 Oe) with respect to $CoFe_2O_4$ (6.4 Oe). Both samples exhibit negligible M_r (*i.e.*, below 0.5 emu·g^{-1}) [24,49]. The observed jumps in $CoFe_2O_4$ could be attributed to the coexistence of Co-ferrite and metallic Co phases in the nanoparticles, yielding two different magnetic hardness and reversal fields [63], which is instead absent in $NiFe_2O_4$. The magnetic characterizations reflect the intrinsic differences between the two magnetic ferrite systems, likely influenced by both the distinct cation distributions within the crystal lattice sites and the different morphologies and particle shapes [24,64].

3.2. Characterization of (magnetic) montmorillonite-based systems

Physicochemical, morphological, structural, textural, and magnetic characterization of (magnetic) montmorillonite-based systems, namely bare montmorillonite, modified montmorillonite, $CoFe_2O_4$/modified-montmorillonite and $NiFe_2O_4$/modified-montmorillonite composites, were performed.

The ATR-FTIR spectra of montmorillonite, modified montmorillonite, and the ferrite–montmorillonite composites are shown in Fig. 3. Pristine montmorillonite displays the characteristic bands associated

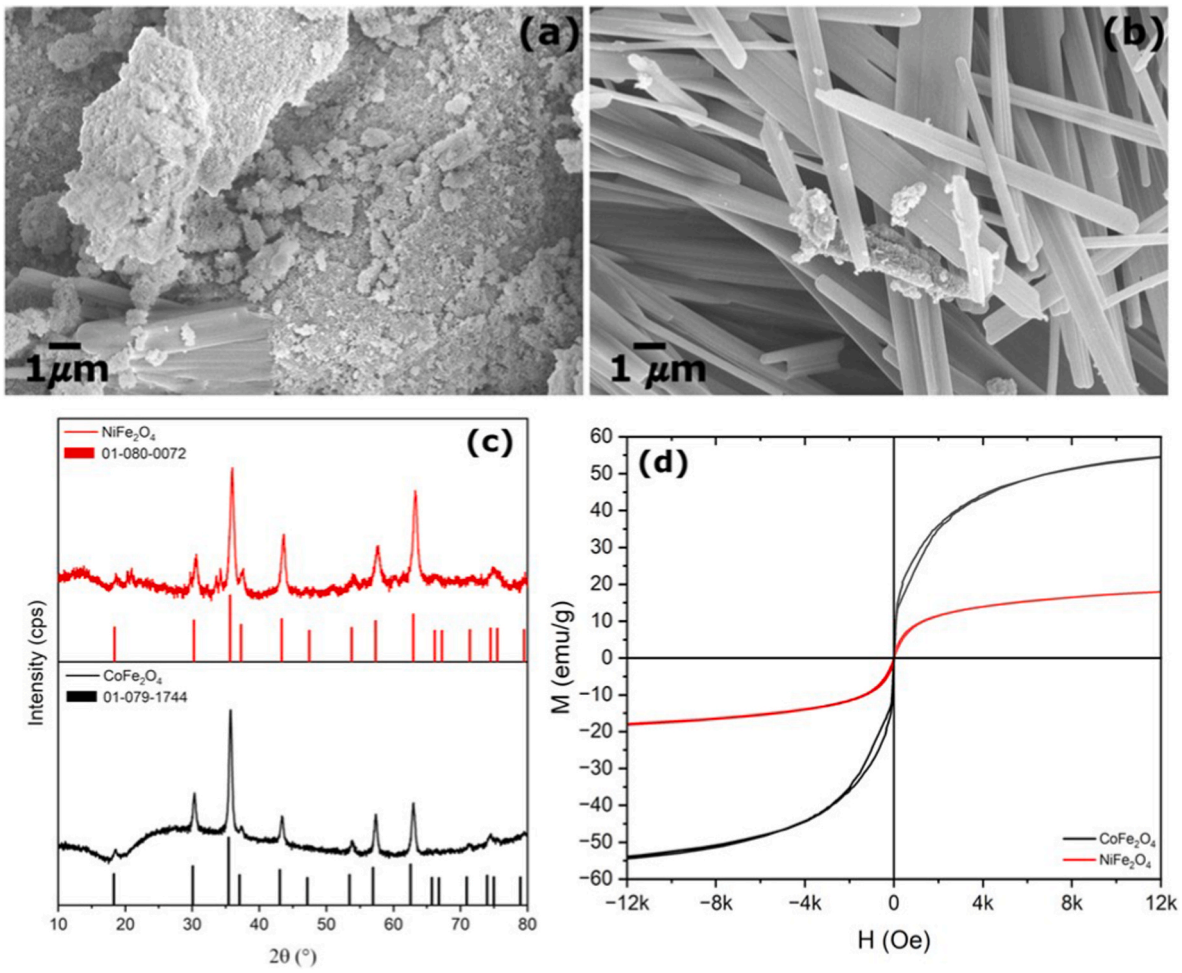

Fig. 2. Characterization of bare ferrite systems. Panels (a,b) SEM micrographs of $CoFe_2O_4$ (a) and $NiFe_2O_4$ (b); micrographs were collected at the same magnification (30k×). Panel (c) XRPD patterns of $CoFe_2O_4$ (black) and $NiFe_2O_4$ (red). XRPD reference patterns: $CoFe_2O_4$ (01-079-1744, black) and $NiFe_2O_4$ (01-080-0072, red). Panel (d) Magnetization curves (M vs. H) of $CoFe_2O_4$ (black) and $NiFe_2O_4$ (red). An enlarged view of the central section of the hysteresis loops is provided in Fig. S2. (For interpretation of the references to colour in this figure legend, the reader is referred to the Web version of this article.)

Table 1
Crystallite average sizes, lattice parameters, BET SSA, and magnetic properties measured at RT for both bare magnetic ferrite systems.

Samples	Crystallite average size (nm)	Lattice parameter (Å) a = b = c	SSA ($m^2 \cdot g^{-1}$)	M_s (emu·g^{-1})	H_c (Oe)	M_r (emu·g^{-1})
$CoFe_2O_4$	18	8.3	16	55.6	2.7	0.2
$NiFe_2O_4$	12	8.3	22	18.8	17.4	0.5

with Si–O stretching vibrations (at *ca.* 1100–1000 cm^{-1}), Al–OH bending (at *ca.* 910 cm^{-1}), and a broad O–H stretching (at *ca.* 3400 cm^{-1}) related to structural hydroxyl groups and interlayer water [65]. Upon organic modification, new signals appear in the region of 2950–2850 cm^{-1}, corresponding to C–H stretching vibrations, thus validating the successful grafting of organosilane groups onto the clay matrix [66].

Regarding the ferrite–montmorillonite composites, both $CoFe_2O_4$/modified-montmorillonite and $NiFe_2O_4$/modified-montmorillonite retain the main clay absorption bands. Overall, the ATR-FTIR analysis verifies both the organic modification of montmorillonite and the successful integration of spinel ferrites, leading to the formation of magnetic ferrite/organoclay systems.

Fig. 4 shows SEM micrographs of the montmorillonite-based systems, revealing significant morphological differences between the unmodified and modified samples. In particular, bare montmorillonite (Fig. 4A and A') exhibits the characteristic layered, plate-like structure, forming compact aggregates with irregular surfaces that become more noticeable at higher magnification, reflecting the intrinsic nature of the silicate layers [67]. In addition, its surface appears rough, composed of both fine and coarse particles, with noticeable roughness and poorly defined boundaries between particle clusters. Upon modification (Fig. 4B and B'), the clay shows partial exfoliation and increased surface roughness, which indicates loosening of the stacked layers. Compared to the unmodified sample, the particles seem more consolidated with fewer loose aggregates.

SEM analysis of (magnetic) montmorillonite-based systems reveals clear morphological changes induced by the presence of the clay. In the $CoFe_2O_4$/modified-montmorillonite composite (Fig. 4C and C'), nanoparticles are dispersed across the clay surface, forming loosely bound aggregates with some degree of agglomeration. The consequence of this is a more porous and fragmented morphology, with evident exfoliated flakes and a sponge-like texture, suggesting enhanced dispersion compared to the granular structure of pure $CoFe_2O_4$. In contrast, in the $NiFe_2O_4$/modified-montmorillonite composite (Fig. 4D and D'), the nanorod structure of pure $NiFe_2O_4$ is no longer evident. Instead, the

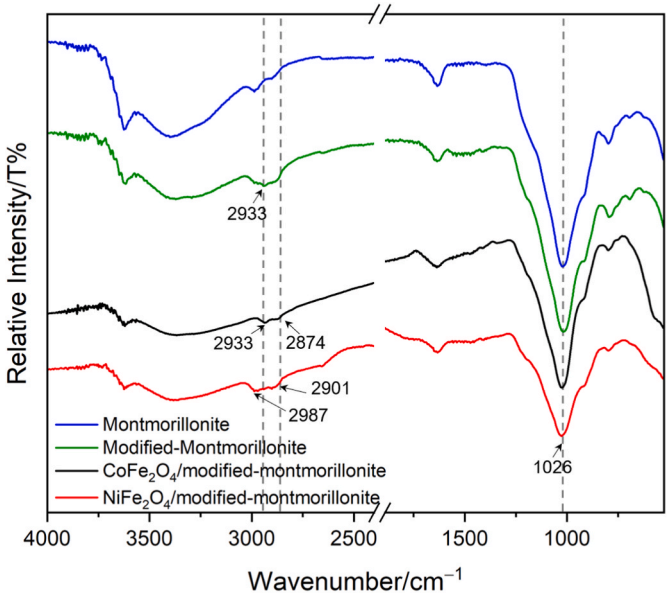

Fig. 3. ATR-FTIR spectra of montmorillonite (blue line), modified-montmorillonite (green line), $CoFe_2O_4$/modified-montmorillonite composite (black line), and $NiFe_2O_4$/modified-montmorillonite composite (red line). (For interpretation of the references to colour in this figure legend, the reader is referred to the Web version of this article.)

sample displays a more homogeneous distribution of nanoparticles, with smaller clusters and reduced aggregation, indicating better dispersion within the support. This disruption of the original morphology may result from interfacial interactions during synthesis, leading to partial fragmentation or restructuring within the layered clay environment [68].

Fig. 5 reports the structural XRPD analysis of montmorillonite and magnetic montmorillonite-based composite systems. In the XRPD patterns of the bare montmorillonite and modified-montmorillonite samples, an intense diffraction peak appears at *ca.* 8.8° 2θ, indicating the presence of dioctahedral phyllosilicates, characteristic of montmorillonite, among the other main reflections at 2θ = 19.9° (002), 35.0° (107), 54.2° (0013), 62.0° (2011), 71.1° (308) (card number 00-029-1499, ICDD) [69]. Additionally, the existence of a diffraction peak at 26.6° 2θ (together with other minor signals) suggests the presence of quartz as a secondary phase (card number 01-082-0511, ICDD) [70]. Moreover, since montmorillonite possesses a hexagonal structure, the lattice parameters *a* and *b* are the same (*ca.* 5 Å), whereas *c* is different (*ca.* 15 Å). From the structural viewpoint, the crystallite size and lattice parameters of bare montmorillonite and modified montmorillonite are similar to each other (*ca.* 60 nm), see Table 2. The magnetic montmorillonite-based composite systems confirm the presence of montmorillonite (card number 00-013-0135, ICDD), as well as the $CoFe_2O_4$ (card number 01-079-1744, ICDD) and $NiFe_2O_4$ (card number 01-080-0072, ICDD). These results confirm the successful incorporation of both ferrite crystal phases into the layered clay while preserving the crystalline identity of both components.

Comparing the structural parameters between the bare $CoFe_2O_4$ and its montmorillonite-modified counterpart ($CoFe_2O_4$/modified-montmorillonite composite), crystallite size remains essentially unchanged, with values of *ca.* 18-19 nm. A similar trend is observed for the $NiFe_2O_4$ and its montmorillonite-modified counterpart ($NiFe_2O_4$/modified-montmorillonite composite) with an analogous crystallite average size (*ca.* 11-12 nm). Interestingly, the lattice parameters of both ferrite-modified-montmorillonite composites closely resemble those of the corresponding pure ferrites, suggesting that the clay modification does not significantly distort the spinel lattice, as expected. On the contrary, when comparing crystallite average sizes among the montmorillonite-based systems, an increase is observed, from 58 nm to 72 nm (for $CoFe_2O_4$/modified-montmorillonite composite) and 66 nm (for the $NiFe_2O_4$/modified-montmorillonite composite), even if the lattice parameters remain nearly constant.

The N_2 adsorption–desorption isotherms are presented in Fig. S4. All samples display characteristic type IV isotherms, as classified by IUPAC, which are typically associated with mesoporous structures. Montmorillonite, modified-montmorillonite, and $CoFe_2O_4$/modified-montmorillonite composites exhibit a pronounced H3-type hysteresis loop in the relative pressure range of 0.4-1.0, suggesting the presence of slit-like pores arising from the layered morphology of the clay. In contrast, $NiFe_2O_4$/modified-montmorillonite composite displays H2-type hysteresis loops characterized by ink-bottle type mesoporosity. The SSA, determined from the BET model, is summarized in Table 2. Bare montmorillonite exhibits a relatively high surface area (218 $m^2\ g^{-1}$), consistent with its typical lamellar and porous nature [71], whereas modified montmorillonite shows a drastic decrease of the SSA to 85 $m^2\ g^{-1}$, in agreement with the SEM images [72]. Interestingly, in the case of magnetic ferrite/modified montmorillonite composite samples, a further decrease of the SSA is observed, reaching 68 $m^2\ g^{-1}$ for $CoFe_2O_4$/modified-montmorillonite composite and 74 $m^2\ g^{-1}$ for $NiFe_2O_4$/modified-montmorillonite composite, respectively [73,74].

The analysis of the magnetic properties shows notable differences among the pure ferrites and the ferrite/modified montmorillonite composites. In particular, the incorporation of ferrite with modified montmorillonite slightly affects the M_s, H_c, and M_r values. The magnetization hysteresis curve profiles are reported in Fig. 6, whereas magnetic parameters are listed in Table 3.

In the case of $CoFe_2O_4$/modified-montmorillonite composite, the sample presents the presence of a hysteresis loop with relevant coercivity and remanence values, thus suggesting a certain level of ferrimagnetism and stronger interparticle interactions compared to $NiFe_2O_4$ modified-montmorillonite sample, which instead seems more paramagnetic [44] (Fig. 6) as its non-modified counterpart. The increase of the minor loops in the $CoFe_2O_4$/modified-montmorillonite composite with respect to the bare ferrite could be ascribed to a phase separation between $CoFe_2O_4$-based and other phases, with an increase of the magnetically harder fraction of the compound or to exchange-biased effects between adjacent particles [75]. As reported in Table 3, both ferrite/modified-montmorillonite composites present lower M_s values compared to their bare ferrite counterparts, with both $CoFe_2O_4$/modified-montmorillonite and $NiFe_2O_4$/modified-montmorillonite composites displaying M_s values of *ca.* 49.5 emu·g^{-1} and *ca.* 12.0 emu·g^{-1}, respectively. Interestingly, for the $CoFe_2O_4$/modified-montmorillonite composite, a noticeable increase in M_r (*ca.* 6.3 emu·g^{-1}) is observed compared to bare $CoFe_2O_4$ (*ca.* 0.2 emu·g^{-1}). On the contrary, both $NiFe_2O_4$/modified-montmorillonite and bare ferrite exhibit negligible M_r values. Overall, magnetic results suggest that the incorporation of ferrites into montmorillonite reduces M_s values due to the dilution effect caused by the presence of a non-magnetic counterpart. The distinct magnetic responses between the two magnetic composites can be attributed to differences in ferrite loading, chemical nature, and particles' morphology of the two starting ferrite systems [76].

3.3. Sorption performances by UV-Vis kinetics and isotherm fitting

The adsorption performance of the magnetic ferrites and montmorillonite-based composite systems for MB dye was assessed by dispersing a fixed amount of each material (10 mg) in 20 mL of a 5 mg L^{-1} MB solution. To prevent interference from suspended magnetic particles during sampling, ferrite powders were magnetically separated before performing the UV–Vis analysis. The experimental evidence of the recovery capability of composite systems by applying an external magnetic field is reported in Fig. S5.

All adsorption tests were performed at neutral pH (pH = 7) to evaluate the materials under environmentally relevant conditions. It is

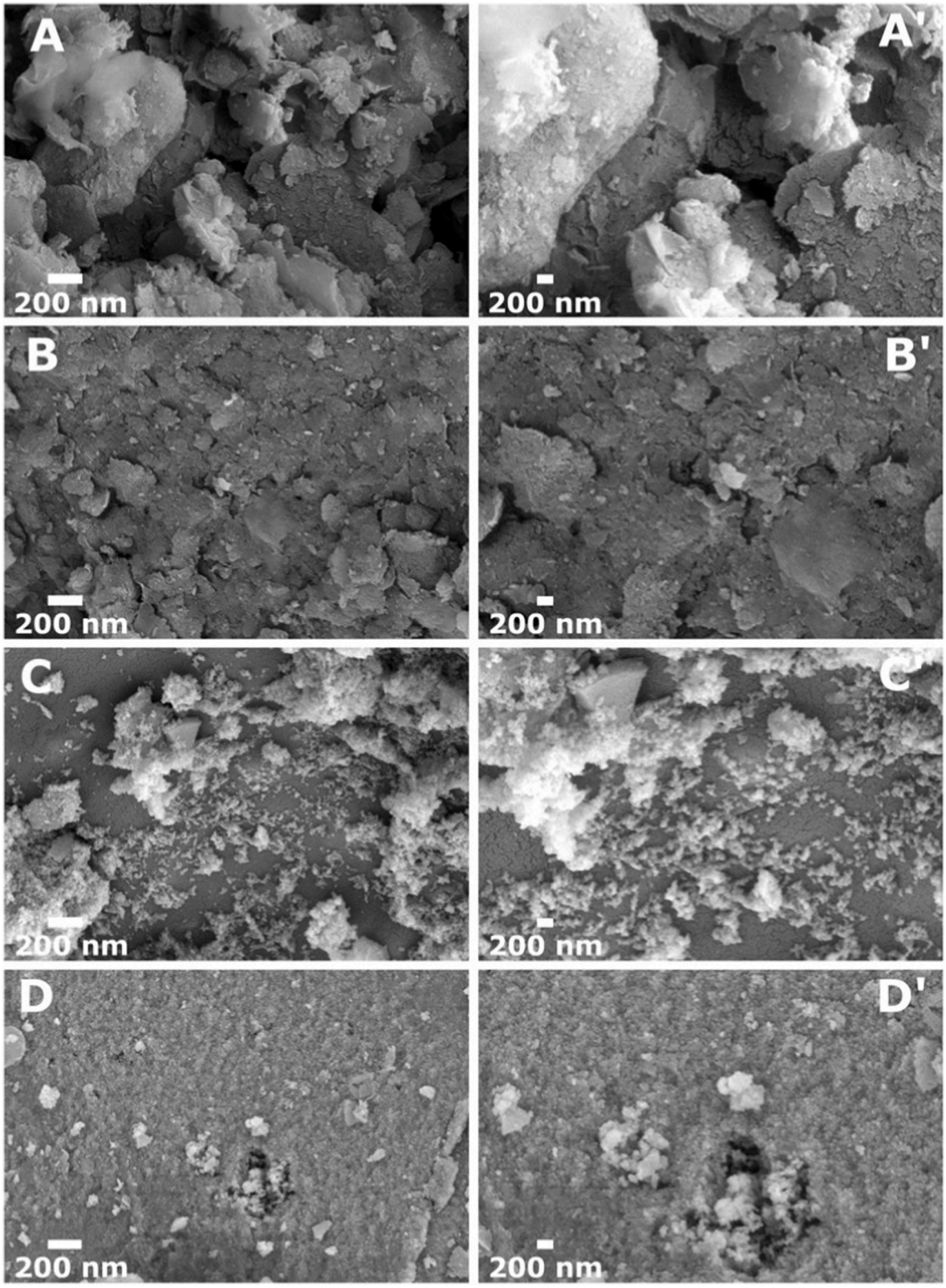

Fig. 4. SEM micrographs of bare montmorillonite (A, A′), modified-montmorillonite (B, B′), $CoFe_2O_4$/modified-montmorillonite composite (C, C′), and $NiFe_2O_4$/modified-montmorillonite composite (D, D′). Micrographs were collected at same magnifications, namely at low (50k ×, left) and high (100k ×, right) magnifications.

well-known that for cationic dyes like MB, an increase in pH typically favors adsorption due to enhanced electrostatic interactions with the deprotonated surface sites, while acidic conditions may inhibit the process, resulting in the dissolution of the ferrite component. The stable performance observed at neutral pH suggests that these composites are effective without requiring any pH adjustment.

As summarized in Fig. 7, after 24 h of contact, the $CoFe_2O_4$ and $NiFe_2O_4$ ferrites exhibit an MB removal efficiency of 33.7% and 27.6%,

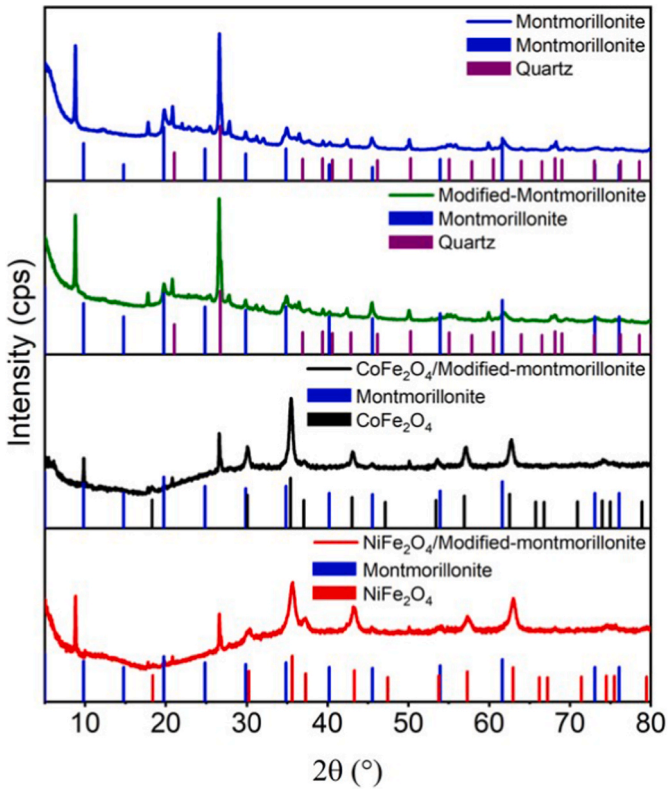

Fig. 5. XRPD patterns of bare montmorillonite (blue), modified-montmorillonite (green), $CoFe_2O_4$/modified-montmorillonite composite (black), and $NiFe_2O_4$/modified-montmorillonite composite (red). XRPD reference patterns: montmorillonite (00-013-0135, blue), quartz (01-082-0511, purple), $CoFe_2O_4$ (01-079-1744, black), and $NiFe_2O_4$ (01-080-0072, red). (For interpretation of the references to colour in this figure legend, the reader is referred to the Web version of this article.)

corresponding to adsorption capacities of 3.58 mg g^{-1} and 2.93 mg g^{-1}, respectively. In contrast, the $CoFe_2O_4$/modified-montmorillonite and $NiFe_2O_4$/modified-montmorillonite composites show significantly enhanced adsorption behavior, achieving an MB removal efficiency of 50.6% and 88.5%, corresponding to adsorption capacities of 4.73 mg g^{-1} and 8.29 mg g^{-1}, respectively. The improved performance of the composites can be attributed to the synergistic effect between the magnetic ferrite nanoparticles and the organically modified montmorillonite matrix, which increases the availability of active adsorption sites and facilitates dye–surface interactions.

The adsorption kinetics of MB onto both $CoFe_2O_4$/modified-montmorillonite and $NiFe_2O_4$/modified-montmorillonite were investigated to elucidate the rate and mechanism of the adsorption process. The temporal profiles of adsorption capacity (q_t; expressed in mg·g^{-1}) as a function of contact time (t; expressed in min) were employed to fit different kinetic models (Eq. 3 and 4, Fig. 8).

To interpret the kinetic behavior, the pseudo-first-order (PFO) and pseudo-second-order (PSO) models were applied. The PFO model is commonly used to describe adsorption systems dominated by physisorption phenomena, where the rate of occupation of adsorption sites is proportional to the number of unoccupied sites. Conversely, the PSO model assumes that the rate-limiting step may involve electron sharing or exchange between adsorbent and adsorbate, making it suitable for systems where chemisorption or stronger surface interactions contribute significantly to the overall adsorption rate. The goodness of fit was assessed by comparing the calculated equilibrium adsorption capacities (q_e) with experimental values and by analyzing the coefficient of determination (R^2) (Table 4).

For the $CoFe_2O_4$/modified-montmorillonite composite, the experimental equilibrium adsorption capacity ($q_{e,exp}$ = 4.74 mg g^{-1}) closely agrees with the value predicted by the PSO model (q_e = 5.10 mg g^{-1}), whereas a slightly larger deviation is observed for the PFO model (q_e = 4.51 mg g^{-1}). The superiority of the PSO model is further confirmed by its higher coefficient of determination (R^2 = 0.9642), in comparison to PFO model (R^2 = 0.9243). Despite that, these findings indicate that the adsorption of MB onto this composite is governed by a kinetic mechanism consistent with both PFO and PSO behavior, suggesting the involvement of both weaker and stronger interactions between the dye molecules and the active sites of the modified montmorillonite [77].

A similar trend is observed for the $NiFe_2O_4$/modified-montmorillonite composite, where the experimental $q_{e,exp}$ (8.29 mg g^{-1}) is nearly identical to that predicted by the PSO model (8.36 mg g^{-1}). The PFO model provides a slightly lower value (7.98 mg g^{-1}). Most notably, the PSO model displays an excellent correlation (R^2 = 0.9992), higher than that of the PFO model (R^2 = 0.9931). This high quality of fit highlights that the adsorption kinetics are driven again by both pseudo-first- and second-order mechanisms, thus indicating the relevance of surface-mediated interactions and possibly chemisorption phenomena.

Overall, both materials exhibit kinetic behavior best described by the PSO model, pointing toward a rate-controlling step associated with surface interactions rather than simple mass transfer or physisorption. The higher adsorption capacity and superior kinetic fit observed for the $NiFe_2O_4$-based composite further suggest a stronger interaction between particles and MB, likely due to differences in surface charge distribution, availability of active sites, or specific adsorbent–adsorbate interactions enhanced by the presence of $NiFe_2O_4$.

To further investigate the rate-controlling step, the intraparticle diffusion model was also evaluated. However, the preliminary testing yielded low correlation coefficients (ranging from 0.44 to 0.89 for the $NiFe_2O_4$-based and $CoFe_2O_4$-based composites, respectively), suggesting that the mass transfer within the pores is not the primary rate-controlling factor relative to the surface adsorption mechanisms. The high correlation for the PSO model confirms that the overall adsorption rate is primarily governed by the chemical interaction between the MB dye and the available active sites (*i.e.*, amines and silanols) on the hybrid sol-gel matrix, rather than by diffusion through the boundary layer or the internal pore structure.

To gain insight into the equilibrium adsorption behavior of MB dye on both $CoFe_2O_4$/modified-montmorillonite and $NiFe_2O_4$/modified-montmorillonite composites, adsorption isotherms were developed

Table 2
Crystallite average size, lattice parameters, and SSA values for bare montmorillonite, modified-montmorillonite, and magnetic montmorillonite-based composite systems.

Samples	Crystallite average size (nm)		Lattice parameters (Å)			SSA ($m^2 \cdot g^{-1}$)
	Montmorillonite	Ferrite	Montmorillonite		Ferrite	
			a = b	c	a = b = c	
Bare montmorillonite	58	–	5.2	15.0	–	218
Modified-montmorillonite	59	–	5.1	14.9	–	85
$CoFe_2O_4$/modified-montmorillonite composite	72	19	5.1	15.1	8.4	68
$NiFe_2O_4$/modified-montmorillonite composite	66	11	5.1	14.7	8.3	74

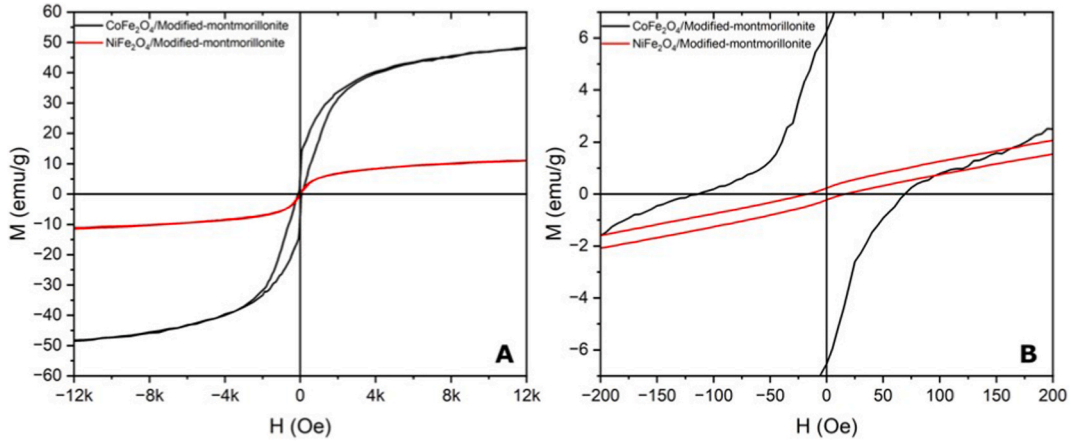

Fig. 6. Magnetization curves M vs. H of magnetic ferrite/modified-montmorillonite composite systems (A, left). Magnetization curves enlarged area to highlight the middle section of the hysteresis loop (B, right). Legend: $CoFe_2O_4$/modified-montmorillonite composite (black), $NiFe_2O_4$/modified-montmorillonite composite (red). (For interpretation of the references to colour in this figure legend, the reader is referred to the Web version of this article.)

Table 3
Comparison between the magnetic response of bare ferrites and (magnetic) montmorillonite-based composite systems measured at RT.

Samples	M_s ($emu \cdot g^{-1}$)	H_c (Oe)	M_r ($emu \cdot g^{-1}$)
$CoFe_2O_4$	55.6	2.7	0.2
$NiFe_2O_4$	18.8	17.4	0.5
$CoFe_2O_4$/modified-montmorillonite composite	49.5	114.2	6.3
$NiFe_2O_4$/modified-montmorillonite composite	12.0	15.5	0.2

using initial MB concentrations ranging from 1 to 15 mg L^{-1} at 25 °C (see the experimental section). After 24 h of contact, the equilibrium dye concentration (C_e) was measured, and the adsorption capacity at equilibrium (q_e) was plotted as a function of C_e. The experimental data were fitted to the Langmuir (Eq. (5)), Freundlich (Eq. (7)), and Temkin (Eq. (8)) isotherm models to elucidate the adsorption mechanism and surface characteristics of the composite materials (Fig. 9). The isotherm parameters were derived through non-linear regression analysis of the experimental data points. This approach was chosen to maintain the integrity of the experimental results and to provide a direct correlation between the equilibrium concentrations and the adsorption capacity. The consistency of the results across the different models confirms the reliability of the observed adsorption trends for both magnetic composites.

The Langmuir model assumes monolayer adsorption on a homogeneous surface with a finite number of identical sites, providing the theoretical maximum adsorption capacity (q_m). In contrast, the Freundlich model describes adsorption on heterogeneous surfaces and allows multilayer formation, with 1/n signifying the adsorption favorability and surface heterogeneity [78]. The Temkin model considers adsorbent–adsorbate interactions and a linear decrease of the heat of adsorption with the surface coverage [79]. The model that best represents the system was identified by comparing the coefficients of determination (R^2) and the agreement between calculated and experimental parameters (Table 5).

For the $CoFe_2O_4$/modified-montmorillonite composite, the Langmuir model provides a good fit to the experimental data, with an R^2 value of 0.9492 and a theoretical maximum adsorption capacity (q_m) of 8.46 mg g^{-1}. This suggests that MB adsorption on this composite tends toward monolayer coverage on relatively uniform active sites. However, the Freundlich model also yields a reasonably high R^2 value (0.8669), with a 1/n value of 0.5499, indicating a moderately heterogeneous surface and a favorable adsorption process. The Temkin model ($R^2 = 0.9422$) further supports the presence of appreciable adsorbent–adsorbate interactions, reflected by the Temkin constant $B_T = 1.853$ J mol^{-1}. Although all three models show acceptable correlation, the Langmuir model appears to best describe the equilibrium behavior, highlighting the prevalence of monolayer adsorption on the modified montmorillonite surface in the presence of $CoFe_2O_4$.

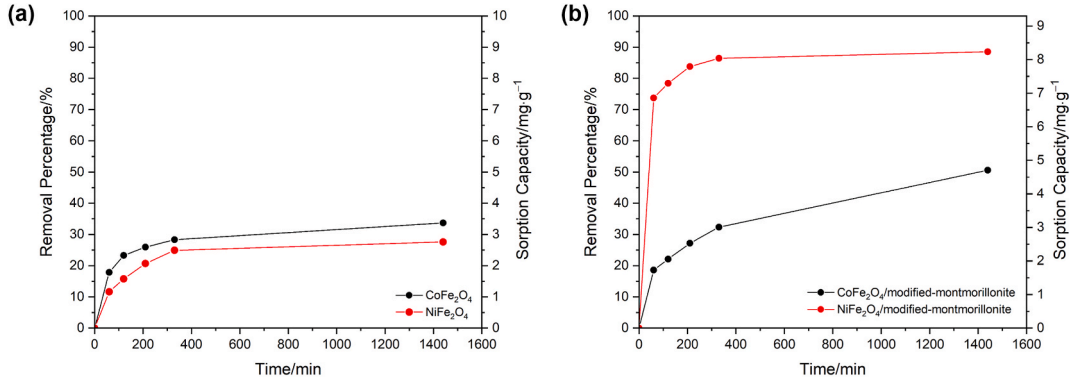

Fig. 7. Plots showing the removal percentage (left vertical axis) and sorption capacity (right vertical axis) of pristine ferrites (a), and montmorillonite-based composite systems (b), at different contact times. Conditions: [sorbent] = 10 mg, [MB dye solution] = 5 mg · L^{-1}, V_{tot} = 20 mL. Legend: $CoFe_2O_4$ and $CoFe_2O_4$/modifed-montmorillonite composite (black), $NiFe_2O_4$ and $NiFe_2O_4$/modified-montmorillonite composite (red). (for interpretation of the references colour in this figure legend, the reader is referred to the Web version of this article.)

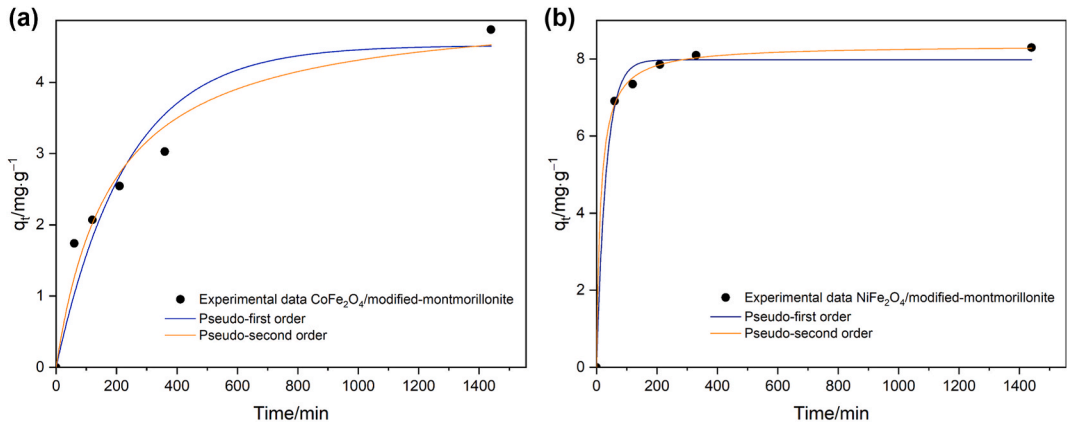

Fig. 8. Plot of the adsorption capacity of MB by $CoFe_2O_4$/modified-montmorillonite (a) and $NiFe_2O_4$/modified-montmorillonite (b), as a function of time, together with kinetic models fitting.

Table 4
Adsorption kinetic rate constants for different applied mechanism models for the adsorption of MB by montmorillonite-based composite systems.

Samples	Experimental data	Kinetic models[a]					
		Pseudo-first order			Pseudo-second order		
	$q_{e,exp}$ (mg•g^{-1})	q_e (mg·g^{-1})	k_1 (min^{-1})	R^2	q_e (mg·g^{-1})	k_2 (g mg^{-1} min^{-1})	R^2
$CoFe_2O_4$/modified-montmorillonite	4.74	4.51	0.0043	0.9243	5.10	0.00107	0.9642
$NiFe_2O_4$/modified-montmorillonite	8.29	7.98	0.0314	0.9931	8.36	0.0089	0.9992

[a] *Note*: See Eq. (3) and Eq. (4).

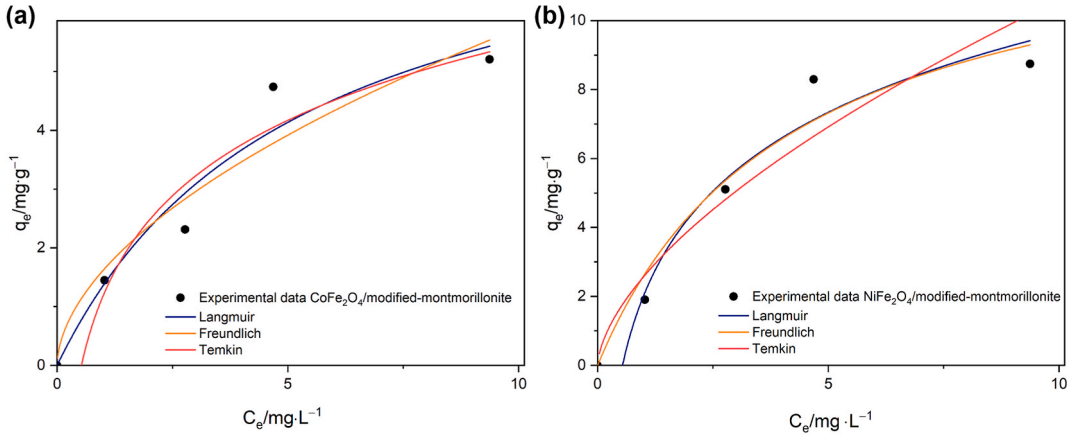

Fig. 9. Plot showing the adsorption capacities of $CoFe_2O_4$/modified-montmorillonite (a) and $NiFe_2O_4$/modified-montmorillonite (b), as a function of different MB equilibrium concentrations, together with isotherm models fitting.

Table 5
Isotherm equilibrium constants for different applied fitting models relative to the adsorption of MB by montmorillonite-based composite systems.

Samples	Adsorption models[a]									
	Langmuir				Freundlich			Temkin		
	q_m (mg·g^{-1})	k_L (L·mg^{-1})	R^2	R_L	1/n	k_F (L·g^{-1})	R^2	B_T (J·mol^{-1})	k_T (L·mg^{-1})	R^2
$CoFe_2O_4$/modified-montmorillonite	8.459	0.1914	0.9492	0.297	0.5499	1.617	0.8669	1.853	1.899	0.9422
$NiFe_2O_4$/modified-montmorillonite	13.44	0.2393	0.9603	0.253	0.6152	2.569	0.8735	3.304	1.844	0.9671

[a] *Note*: See Eqs. (5)–(8).

In contrast, the $NiFe_2O_4$/modified-montmorillonite composite exhibits a higher affinity toward MB, with a Langmuir q_m value of 13.44 mg g^{-1}, significantly exceeding that of the Co-based analogue. Among the tested isotherms, the Temkin model provides the best fit (R^2 = 0.9671), suggesting that adsorbent–adsorbate interactions and variations in adsorption energy play a more dominant role in this system. The corresponding Temkin constant B_T (3.304 J mol^{-1}) is markedly higher than that of the $CoFe_2O_4$-based material, indicating stronger interactions between MB molecules and the $NiFe_2O_4$ composite. The Langmuir and Freundlich models also correlate reasonably well

($R^2 = 0.9603$ and 0.8735, respectively), with the Freundlich 1/n value of 0.6152, further confirming a favorable, though heterogeneous, adsorption process. The overall results suggest that the $NiFe_2O_4$-modified composite follows a mixed adsorption mechanism, characterized by both monolayer formation and energetically variable adsorption sites, with a more pronounced interaction energy profile than the Co-containing system.

Taken together, these findings show that both composites exhibit favorable MB adsorption, with slightly different surface behaviors. In particular, the $CoFe_2O_4$/modified-montmorillonite system is more consistent with Langmuir-type monolayer adsorption, while $NiFe_2O_4$/modified-montmorillonite displays an adsorption process better represented by the Temkin model, indicating stronger dye–surface interactions and a more energetically heterogeneous adsorption environment.

To confirm the favorability of the adsorption process, the dimensionless separation factor (R_L) was calculated using Eq. (6). The values obtained were 0.297 for the $CoFe_2O_4$-based composite and 0.253 for the $NiFe_2O_4$ analogue. Both values are between 0 and 1, thus indicating quantitative evidence of a favorable adsorption of MB on these magnetic hybrid substrates and indicating a strong affinity between the dye molecules and the functionalized organoclay surface.

As highlighted in the comparative analysis presented in Table 6 [44, 80–83], the maximum adsorption capacities (q_m) obtained in this study (8.46 and 13.44 mg g^{-1}) are significantly higher than those reported for similar pristine ferrite systems synthesized via simpler routes, such as the grinding method (1.9–3.6 mg g^{-1}). While some literature reports, often involving complex bio-polymeric composites (*i.e.*, chitosan-blended, starch) [84] or specific alkaline conditions (*e.g.*, pH 10), show higher absolute uptake values. It is important to emphasize that the materials developed in this work achieve competitive performance under neutral conditions (pH 7), which is more representative of realistic wastewater scenarios, within a robust sol-gel framework. This specific architecture prioritizes structural stability and magnetic recoverability, ensuring that the functional sites remain anchored without the leaching issues that are typical in surfactant-rich or purely physically blended systems. Furthermore, this stable host matrix facilitated a distinct differentiation between the performance of $CoFe_2O_4$ and $NiFe_2O_4$, revealing fundamentally different adsorption mechanisms (*i.e.*, Langmuir vs. Temkin). This distinction provides deeper insight into how the specific choice of the magnetic spinel filler influences the surface energy distribution and the overall behavior of hybrid network.

4. Conclusions

In the present study, magnetic ferrite/organoclay composite systems were prepared by introducing either $CoFe_2O_4$ or $NiFe_2O_4$ magnetic particles through intercalation into an organically modified montmorillonite clay functionalized by two alkoxysilanes. The effectiveness of the synthesis of these magnetic composites was monitored by means of many physicochemical (ATR-FTIR spectroscopy), morphological (SEM), structural (XRPD, BET isotherms), and magnetic (VSM) characterization techniques. Lastly, both pristine magnetic ferrites and ferrite/organoclay composites were tested as sorbents for the removal of Methylene Blue (MB) dye from an aqueous matrix. Experimental and model-predicted results demonstrated that.

- Pristine $CoFe_2O_4$ and $NiFe_2O_4$ exhibited a MB removal efficiency (adsorption capacity) of 33.7% (3.58 mg g^{-1}) and 27.6% (2.93 mg g^{-1}), respectively. Interestingly, $CoFe_2O_4$/modified-montmorillonite and $NiFe_2O_4$/modified-montmorillonite composites exhibited an enhanced adsorption behavior, achieving an MB removal efficiency (adsorption capacity) of 50.6% (4.73 mg g^{-1}) and 88.5% (8.29 mg g^{-1}), respectively.
- In kinetic studies that were carried out on both $CoFe_2O_4$/modified-montmorillonite and $NiFe_2O_4$/modified-montmorillonite composites, the MB adsorption is governed by a kinetic mechanism consistent with both pseudo-first-order (PFO) and pseudo-second-order (PSO) behaviors, thus suggesting the involvement of both weak and strong interactions (chemisorption) between the dye molecules and the available active sites, with a prevalence of the pseudo-second-order model, characterized by a rate-controlling step associated with surface interactions.
- In equilibrium adsorption isotherm studies, the behavior of $CoFe_2O_4$/modified-montmorillonite composite (theoretical maximum adsorption capacity (q_m) of 8.46 mg g^{-1}) is more accurately described by the Langmuir model, suggesting a tendency toward a monolayer coverage on relatively uniform active sites, whereas the behavior of $NiFe_2O_4$/modified-montmorillonite composite (q_m value of 13.44 mg g^{-1}) seems better characterized by the Temkin model, suggesting that adsorbent–adsorbate interactions and adsorption energy play a more dominant role in the adsorption mechanism.

In conclusion, this work demonstrates that the rational design of a

Table 6
Comparison of the performances of different developed ferrite-based adsorbent systems.

Functional materials	Synthesis approach	Experimental conditions	Starting MB conc. (mg·L^{-1})	Theoretical maximum adsorption capacity (q_m) (mg·g^{-1})	Ref.
$ZnFe_2O_4$	Grinding method	pH 7, 0.1 g of adsorbent and 100 mL of MB	10–100	3.6	[80]
$CoFe_2O_4$	Grinding method	pH 7, 0.1 g of adsorbent and 100 mL of MB	10–100	1.9	[80]
Montmorillonite/$NiFe_2O_4$@amine-functionalized chitosan composite	Blending	pH 7, 0.05 g of adsorbent, 50 mL of MB, and temperature (25–60 °C)	25	137	[81]
Montmorillonite/$CoFe_2O_4$ and Montmorillonite/starch/$CoFe_2O_4$	Co-precipitation method	pH (2–10), time (10–50 min), composite concentration (0.6–1.4 g L^{-1}), and temperature (25–45 °C)	5–25	Montmorillonite/$CoFe_2O_4$: 36.91 and Montmorillonite/starch/$CoFe_2O_4$: 43.95	[44]
$CoFe_2O_4$@Kaolinite	Co-precipitation method	pH (2–10), adsorbent dose (0.2–1.2 g L^{-1}), and temperature (25–55 °C)	10–500	175.28 (at pH 10)	[82]
Fe_3O_4/kaolinite (the obtained samples are labelled as KAFE-x, where x is the mass percentage of Fe_3O_4)	Solid state reaction method	pH (2–10), 0.05 g of adsorbent and 20 mL of MB	25–400	KAFE-7: 42.3 KAFE-30: 14.3	[83]
$CoFe_2O_4$/modified-montmorillonite	Sol-gel and ultrasound intercalation	pH 7, 0.01 g of adsorbent and 20 mL of MB	1–15	8.46	This work
$NiFe_2O_4$/modified-montmorillonite	Sol-gel and ultrasound intercalation	pH 7, 0.01 g of adsorbent and 20 mL of MB	1–15	13.44	This work

covalent sol-gel network is a viable strategy to integrate magnetic ferrites into clay structures. The novelty lies not merely in the adsorption capacity, but in the creation of a chemically stable and magnetically responsive platform where the choice of the spinel ferrite allows for the tuning of the adsorption mechanism, moving from monolayer coverage to energy-distributed interactions. Although the maximum adsorption capacities are lower than those reported for some surfactant-rich systems, the developed composites offer superior practical competitiveness due to their structural integrity, which prevents the leaching of organic modifiers, and their good magnetic responsive nature, which facilitates rapid and low-cost recovery from treated water.

These very interesting and promising adsorption results, coupled with the intrinsic magnetic properties shown by these composite materials, clearly suggested the potential application of these sorbing systems in environmental remediation processes involving the bonification of contaminated aqueous media. Moreover, although the kinetic and isotherm models point toward a mechanism dominated by surface interactions and chemisorption phenomena, additional spectroscopic studies, such as post-adsorption XPS, could be carried out in future work to provide direct evidence of the chemical linkages and coordination environments between the dye molecules and the hybrid sol-gel matrix. Furthermore, while the magnetic properties of the composites were successfully demonstrated, additional experimental tests are required to optimize the regeneration protocols (*e.g.*, using specific matrices or pH adjustments) and to evaluate the retention of adsorption capacity over multiple cycles. The high structural stability of the sol-gel framework presented here provides a promising foundation for these future reusability tests. Therefore, future developments of this work will focus on evaluating the preservation of the adsorption performance of the magnetic ferrite/organoclay composites over multiple adsorption–desorption cycles, to assess their reusability, structural stability, and long-term effectiveness as sustainable and magnetically recoverable sorbents for water remediation applications.

CRediT authorship contribution statement

Giulia Rando: Data curation, Formal analysis, Investigation, Writing – original draft, Writing – review & editing. **Tatiana Rodriguez-Flores:** Data curation, Formal analysis, Investigation, Writing – original draft, Writing – review & editing. **Silvia Sfameni:** Data curation, Formal analysis, Investigation, Writing – review & editing. **Falak Shafiq:** Data curation, Formal analysis, Investigation, Writing – review & editing. **Matteo Cantoni:** Data curation, Formal analysis, Investigation, Resources, Writing – review & editing. **Maria Rosaria Plutino:** Conceptualization, Data curation, Formal analysis, Funding acquisition, Investigation, Resources, Supervision, Writing – original draft, Writing – review & editing. **Roberto Nisticò:** Conceptualization, Data curation, Formal analysis, Funding acquisition, Investigation, Resources, Supervision, Writing – original draft, Writing – review & editing.

Declaration of competing interest

The authors declare that they have no known competing financial interests or personal relationships that could have appeared to influence the work reported in this paper.

Acknowledgements

CNR and MUR are gratefully acknowledged. This work received financial support from MUR (Italy) and the European Union – Next Generation EU, Mission 4, Component 1, CUP (H53D23004490001) through the PRIN Project MAPEC (N. 2022599NR3), and CUP (H53D23008000001) through the PRIN Project PERFECT (N. P2022TK9B9), which are gratefully acknowledged. T.R.F. would like to acknowledge the Secreteria de Educacion, Ciencia, Tecnologia e Inovacion (Mexico City, Mexico) No. SECTEI/197/2024. Authors would like to acknowledge Dr. Paolo Gentile (University of Milano-Bicocca, Italy) for the technical support during the SEM analysis, and Ms. Sofia Faina (University of Milano-Bicocca, Italy) for the technical support during the BET SSA analysis. This work has been also supported by European Union (NextGeneration EU), through the MUR-PNRR project SAMOTHRACE (SiciliAn MicronanOTecH Research And Innovation Center, ECS00000022) and the MICS (Made in Italy–Circular and Sustainable) Extended Partnership and received funding from the European Union Next-Generation EU (PIANO NAZIONALE DI RIPRESA E RESILIENZA (PNRR) –MISSIONE 4 COMPONENTE 2, INVESTIMENTO 1.3 –D. D. 1551.11-10-2022, PE00000004). This manuscript reflects only the authors' views and opinions; neither the European Union nor the European Commission can be considered responsible for them. BaC ECO-SISTER Spoke 1 - CNR (HG4T - High-performance geopolymer concrete precast elements for tunnel rehabilitation) project is gratefully acknowledged.

Appendix A. Supplementary data

Supplementary data to this article can be found online at https://doi.org/10.1016/j.ceramint.2026.06.336.

References

[1] G.I. Edo, L.O. Itoje-akpokiniovo, P. Pbasohan, V.O. Ikpekoro, P.O. Samuel, A. N. Jikah, L.C. Nosu, H.A. Ekokotu, U. Ugbune, E.E.A. Oghroro, O.L. Emakpor, I. E. Ainyanbhor, W.A. Mohammed, P.O. Akpoghelie, J.O. Owheruo, J.J. Agbo, Impact of environmental pollution from human activities on water, air quality and climate change, Ecol. Front. 44 (2024) 874–889, https://doi.org/10.1016/j.ecofro.2024.02.014.

[2] G. Rando, S. Sfameni, M. Milone, A. Mezzi, M. Brucale, A. Notti, M.R. Plutino, Smart pillar[5]arene-based PDMAEMA/PES beads for selective dye pollutants removal: design, synthesis, chemical-physical characterization, and adsorption kinetic studies, ChemSusChem 17 (2024) e202301502, https://doi.org/10.1002/cssc.202301502.

[3] A. Foglia, J. Gonzalez-Camejo, S. Radini, M. Sgroi, K. Li, A.L. Eusebi, F. Fatone, Transforming wastewater treatment plants into reclaimed water facilities in water-unbalanced regions. An overview of possibilities and recommendations focusing on the Italian case, J. Clean. Prod. 410 (2023) 137264, https://doi.org/10.1016/j.jclepro.2023.137264.

[4] C. Tortajada, A.K. Biswas, Achieving universal access to clean water and sanitation in an era of water scarcity: strengthening contributions from academia, Curr. Opin. Environ. Sustain. 34 (2018) 21–25, https://doi.org/10.1016/j.cosust.2018.08.001.

[5] M. Magni, E.R. Jones, M.F.P. Bierkens, M.T.H. van Vliet, Global energy consumption of water treatment technologies, Water Res. 277 (2025) 123245, https://doi.org/10.1016/j.watres.2025.123245.

[6] Y. Yang, Y.S. Ok, K.-H. Kim, E.E. Kwon, Y.F. Tsang, Occurrences and removal of pharmaceuticals and personal care products (PPCPs) in drinking water and water/sewage treatment plants: a review, Sci. Total Environ. 596–597 (2017) 303–320, https://doi.org/10.1016/j.scitotenv.2017.04.102.

[7] G. Kavitha, M. Govindhan, S. Premkumar, Dye pollution and its implications for human health, aquatic ecosystems, and sustainable wastewater treatment: a comprehensive review, J. Water Proc. Eng. 80 (2025) 109071, https://doi.org/10.1016/j.jwpe.2025.109071.

[8] R. Al-Tohamy, S.S. Ali, F. Li, K.M. Okasha, Y.A.-G. Mahmoud, T. Elsamahy, H. Jiao, Y. Fu, J. Sun, A critical review on the treatment of dye-containing wastewater: ecotoxicological and health concerns of textile dyes and possible remediation approaches for environmental safety, Ecotoxicol. Environ. Saf. 231 (2022) 113160, https://doi.org/10.1016/j.ecoenv.2021.113160.

[9] D. Chen, Y. Cheng, N. Zhou, P. Chen, Y. Wang, K. Li, S. Huo, P. Cheng, P. Peng, R. Zhang, L. Wang, H. Liu, Y. Liu, R. Ruan, Photocatalytic degradation of organic pollutants using TiO_2-based photocatalysts: a review, J. Clean. Prod. 268 (2020) 121725, https://doi.org/10.1016/j.jclepro.2020.121725.

[10] A. Chakravorty, S. Roy, A review of photocatalysis, basic principles, processes, and materials, Sustain. Chem. Environ. 8 (2024) 100155, https://doi.org/10.1016/j.scenv.2024.100155.

[11] M. Priyadarshini, I. Das, M.M. Ghangrekar, L. Blaney, Advanced oxidation processes: performance, advantages, and scale-up of emerging technologies, J. Environ. Manag. 316 (2022) 115295, https://doi.org/10.1016/j.jenvman.2022.115295.

[12] J. Gao, T. Qin, S. Waclawek, X. Duan, Y. Huang, H. Liu, D.D. Dionysiou, The application of advanced oxidation processes (AOPs) to treat unconventional water for fit-for-purpose reuse, Curr. Opin. Chem. Eng. 42 (2023) 100974, https://doi.org/10.1016/j.coche.2023.100974.

[13] S. Ullah, S.S.A. Shah, M. Altaf, I. Hossain, M.E. El Sayed, M. Kallel, Z.M. El-Bahy, A. ur Rehman, T. Najam, M.A. Nazir, Activated carbon derived from biomass for wastewater treatment: synthesis, application and future challenges, J. Anal. Appl. Pyrolysis 179 (2024) 106480, https://doi.org/10.1016/j.jaap.2024.106480.

[14] Y. Dehmani, I. Bentahar, H. Lgaz, A. El-Kordy, A. Aldalbahi, A.A. Alrashdi, A. Dehbi, T. Lamhasni, B. Hammouti, A. Sadik, A critical review of natural clay minerals: structural characterization, textural properties, and adsorption mechanisms for sustainable wastewater treatment, Mater. Today Adv. 29 (2026) 100682, https://doi.org/10.1016/j.mtadv.2025.100682.
[15] H. Xin, J. Ao, Y. Wu, W. Chen, J. Xiao, L. Bu, S. Zhou, Long-chain quaternary ammonium-modified anion exchange resins for selective and high-efficiency perchlorate adsorption from wastewater, Separ. Purif. Technol. 381 (2026) 135592, https://doi.org/10.1016/j.seppur.2025.135592.
[16] A.V. Baskar, N. Bolan, S.A. Hoang, P. Sooriyakumar, M. Kumar, L. Singh, T. Jasemizad, L.P. Padhye, G. Singh, A. Vinu, B. Sarkar, M.B. Kirkham, J. Rinklebe, S. Wang, H. Wang, R. Balasubramanian, K.H.M. Siddique, Recovery, regeneration and sustainable management of spent adsorbents from wastewater treatment streams: a review, Sci. Total Environ. 822 (2022) 153555, https://doi.org/10.1016/j.scitotenv.2022.153555.
[17] M. Hassan, R. Naidu, J. Du, Y. Liu, F. Qi, Critical review of magnetic biosorbents: their preparation, application, and regeneration for wastewater treatment, Sci. Total Environ. 702 (2020) 134893, https://doi.org/10.1016/j.scitotenv.2019.134893.
[18] S.M. Prabhu, N.R. Rane, X. Li, S.V. Otari, S.D. Girawale, A.R. Palake, K.M. Kodam, Y.-K. Park, Y.-H. Ha, K.K. Yadav, M.A. Khan, B.-H. Jeon, Magnetic nanostructured adsorbents for water treatment: Structure-property relationships, chemistry of interactions, and lab-to-industry integration, Chem. Eng. J. 468 (2023) 143474, https://doi.org/10.1016/j.cej.2023.143474.
[19] R. de Jesus Andrade Fidelis, M. Pires, D.S. de Resende, G.F. Costa Lima, P.R.P. de Paiva, A.C. da Silva Bezerra, Magnetite: properties and applications – a review, J. Magn. Magn Mater. 614 (2025) 172770, https://doi.org/10.1016/j.jmmm.2025.172770.
[20] H. Shokrollahi, A review of the magnetic properties, synthesis methods and applications of maghemite, J. Magn. Magn Mater. 426 (2017) 74–81, https://doi.org/10.1016/j.jmmm.2016.11.033.
[21] R. Nisticò, A synthetic guide toward the tailored production of magnetic iron oxide nanoparticles, Bol. Soc. Espanola Ceram. Vidr. 60 (2021) 29–40, https://doi.org/10.1016/j.bsecv.2020.01.011.
[22] D. Hu, R. Han, H. Fei, K. Zheng, B. Zhang, ZVI and ball milling co-modified biochar for chromium (Cr(VI)) removal from groundwater: Performance pptimization and mechanisms, Colloids Surf. A Physicochem. Eng. Asp. 714 (2025) 136574, https://doi.org/10.1016/j.colsurfa.2025.136574.
[23] T. Rodriguez-Flores, F. Shafiq, R. Nisticò, Synthesis, properties, and application in catalysis of Cu, Ni, Co, Zn ferrites: a comprehensive review study, J. Alloys Compd. 1036 (2025) 181926, https://doi.org/10.1016/j.jallcom.2025.181926.
[24] R. Nisticò, R. Mantovan, M. Cantoni, C. Rinaldi, M. Malandrino, S. Mostoni, M. D'Arienzo, B. Di Credico, R. Scotti, Hydrothermal synthesis of Cu-substituted Ni ferrites: structural, morphological, and magnetic properties, J. Alloys Compd. 981 (2024) 173628, https://doi.org/10.1016/j.jallcom.2024.173628.
[25] S.F. Rafie, N. Abu-Zahra, M. Sillanpaa, A comprehensive review of spinel ferrites and their magnetic composites as highly efficient adsorbents of rare earth elements, Emerging Contam. 11 (2025) 100429, https://doi.org/10.1016/j.emcon.2024.100429.
[26] M. Wang, X. You, Critical review of magnetic polysaccharide-based adsorbents for water treatment: synthesis, application and regeneration, J. Clean. Prod. 323 (2021) 129118, https://doi.org/10.1016/j.jclepro.2021.129118.
[27] B. Junlu, H. Pengfei, Z. JunJie, Z. Xiaojun, L. Peipei, Preparation of a separable composite of Fe_3O_4@SiO_2@MnO_2 magnetic submicrospheres as an efficient adsorbent for the highly sensitive determination of tetracyclines in aquatic products, Microchem. J. 212 (2025) 113453, https://doi.org/10.1016/j.microc.2025.113453.
[28] J. Vaz-Ramos, S. Le Calvé, S. Begin, Polycyclic aromatic hydrocarbons in water environments: impact, legislation, depollution processes and challenges, and magnetic iron oxide/graphene-based nanocomposites as promising adsorbent solutions, J. Hazard Mater. 490 (2025) 137726, https://doi.org/10.1016/j.jhazmat.2025.137726.
[29] M. Ahmad, U. Riaz, S. Iqbal, H. Rasheed, M.A. Mousa Mousa, A.S.F. Al-Farraj, M. I. Al-Wabel, Advances in the development and applications of clay-based composites, in: M. Vithanage, G. Lazzara, A.U. Rajapaksha (Eds.), Clay Composites. Advances in Material Research and Technology, Springer Nature Singapore, Singapore, 2023, pp. 75–88, https://doi.org/10.1007/978-981-99-2544-5_4.
[30] P. Aranda, M. Darder, B. Wicklein, G. Rytwo, E. Ruiz-Hitzky, Clay–organic interfaces for design of functional hybrid materials, in: M.-H. Delville, A. Taubert (Eds.), Hybrid Organic-Inorganic Interfaces: towards Advanced Functional Materials, Wiley-VCH Verlag GmbH & Co. KGaA, Weinheim, Germany, 2018, pp. 1–84, https://doi.org/10.1002/9783527807130.ch1.
[31] P. Merghes, G. Ilia, B. Maranescu, N. Varan, V. Simulescu, The sol–gel process, a green method used to obtain hybrid materials containing phosphorus and zirconium, Gels 10 (2024) 656, https://doi.org/10.3390/gels10100656.
[32] A. Maged, H.A. El-Fattah, R.M. Kamel, S. Kharbish, A.M. Elgarahy, A comprehensive review on sustainable clay-based geopolymers for wastewater treatment: circular economy and future outlook, Environ. Monit. Assess. 195 (2023) 693, https://doi.org/10.1007/s10661-023-11303-9.
[33] M. del M. Orta, J. Martín, J.L. Santos, I. Aparicio, S. Medina-Carrasco, E. Alonso, Biopolymer-clay nanocomposites as novel and ecofriendly adsorbents for environmental remediation, Appl. Clay Sci. 198 (2020) 105838, https://doi.org/10.1016/j.clay.2020.105838.
[34] R. Nisticò, A comprehensive study on the applications of clays into advanced technologies, with a particular attention on biomedicine and environmental remediation, Inorganics 10 (2022) 40, https://doi.org/10.3390/inorganics10030040.
[35] T. de Oliveira, M. Boussafir, L. Fougere, E. Destandau, Y. Sugahara, R. Guegan, Use of a clay mineral and its nonionic and cationic organoclay derivatives for the removal of pharmaceuticals from rural wastewater effluents, Chemosphere 259 (2020) 127480, https://doi.org/10.1016/j.chemosphere.2020.127480.
[36] L.B. de Paiva, A.R. Morales, F.R. Valenzuela Diaz, Organoclays: properties, preparation and applications, Appl. Clay Sci. 42 (2008) 8–24, https://doi.org/10.1016/j.clay.2008.02.006.
[37] S. Sfameni, G. Rando, M.R. Plutino, Sustainable secondary-raw materials, natural substances and eco-friendly nanomaterial-based approaches for improved surface performances: an overview of what they are and how they work, Int. J. Mol. Sci. 24 (2023) 5472, https://doi.org/10.3390/ijms24065472.
[38] V. Trovato, S. Sfameni, R. Ben Debabis, G. Rando, G. Rosace, G. Malucelli, M. R. Plutino, How to address flame-retardant technology on cotton fabrics by using functional inorganic sol–gel precursors and nanofillers: flammability insights, research advances, and sustainability challenges, Inorganics 11 (2023) 306, https://doi.org/10.3390/inorganics11070306.
[39] G. Rando, S. Sfameni, M. Hadhri, A. Mezzi, M. Brucale, G. De Luca, E. Piperopoulos, C. Milone, D. Drommi, G. Rosace, V. Trovato, M.R. Plutino, Methyl Red-loaded halloysite nanotubes-based silica coatings for durable dyeing of polyester fabrics, Surf. Interfaces 53 (2024) 105006, https://doi.org/10.1016/j.surfin.2024.105006.
[40] P. Yuan, M. Fan, D. Yang, H. He, D. Liu, A. Yuan, J. Zhu, T. Chen, Montmorillonite-supported magnetite nanoparticles for the removal of hexavalent chromium [Cr (VI)] from aqueous solutions, J. Hazard Mater. 166 (2009) 821–829, https://doi.org/10.1016/j.jhazmat.2008.11.083.
[41] J. Jang, D.S. Lee, Magnetite nanoparticles supported on organically modified montmorillonite for adsorptive removal of iodide from aqueous solution: optimization using response surface methodology, Sci. Total Environ. 615 (2018) 549–557, https://doi.org/10.1016/j.scitotenv.2017.09.324.
[42] R. Haounati, H. Ighnih, R.E. Malekshah, N. Nouj, H. Ouachtak, B. Sljukic, D.M. F. Santos, A. Hsini, A. Shaim, A. Jada, A.A. Addi, Advanced contaminant removal through synergistic interactions of montmorillonite, $CoFe_2O_4$ nanoparticles, and surfactants: combining theoretical and experimental approaches, JJ. Mol. Liq. 428 (2025) 127490, https://doi.org/10.1016/j.molliq.2025.127490.
[43] M.E. Mahmoud, M.A. Khalifa, A.A. Attia, M.W. Helmy, M.A.B. Al-Sherady, Effective adsorptive uptake of hexavalent chromium ions from aqueous systems utilizing a superior activated nanobentonite@cobalt ferrite@carboxymethylcellulose nanocomposite, JJ. Mol. Liq. 407 (2024) 125172, https://doi.org/10.1016/j.molliq.2024.125172.
[44] A. Ahmadi, R. Foroutan, H. Esmaeili, S.J. Peighambardoust, S. Hemmati, B. Ramavandi, Montmorillonite clay/starch/$CoFe_2O_4$ nanocomposite as a superior functional material for uptake of cationic dye molecules from water and wastewater, Mater. Chem. Phys. 284 (2022) 126088, https://doi.org/10.1016/j.matchemphys.2022.126088.
[45] F. Puoci, C. Saturnino, V. Trovato, D. Iacopetta, E. Piperopoulos, C. Triolo, M. G. Bonomo, D. Drommi, O.I. Parisi, C. Milone, M.S. Sinicropi, G. Rosace, M. R. Plutino, Sol-gel treatment of textiles for the entrapping of an antioxidant/anti-inflammatory molecule: functional coating morphological characterization and drug release evaluation, Appl. Sci. 10 (2020) 2287, https://doi.org/10.3390/app10072287.
[46] S. Sfameni, T. Lawnick, G. Rando, A. Visco, T. Textor, M.R. Plutino, Functional silane-based nanohybrid materials for the development of hydrophobic and water-based stain resistant cotton fabrics coatings, Nanomaterials 12 (2022) 3404, https://doi.org/10.3390/nano12193404.
[47] S. Sfameni, T. Lawnick, G. Rando, A. Visco, T. Textor, M.R. Plutino, Super-hydrophobicity of polyester fabrics driven by functional sustainable fluorine-free silane-based coatings, Gels 9 (2023) 109, https://doi.org/10.3390/gels9020109.
[48] S. Sfameni, G. Rando, A. Marchetta, C. Scolaro, S. Cappello, C. Urzì, A. Visco, M. R. Plutino, Development of eco-friendly hydrophobic and fouling-release coatings for blue-growth environmental applications: synthesis, mechanical characterization and biological activity, Gels 8 (2022) 528, https://doi.org/10.3390/gels8090528.
[49] L. De Pasquale, T. Rodriguez-Flores, D. Valenzisi, F. Shafiq, R. Scotti, F. Tavella, M. Cantoni, M.V. Dozzi, C. Genovese, R. Nisticò, Partially substituted magnetic ferrites as Pt-free catalysts for hydrogen evolution from water photo-electrolysis, Dalton Trans. 55 (2026) 4584–4600, https://doi.org/10.1039/D5DT03018H.
[50] H. Moussout, H. Ahlafi, M. Aazza, H. Maghat, Critical of linear and nonlinear equations of pseudo-first order and pseudo-second order kinetic models, Karbala Int. J. Mod. Sci. 4 (2018) 244–254, https://doi.org/10.1016/j.kijoms.2018.04.001.
[51] S.K. Lagergren, About the theory of so-called adsorption of soluble substances, K. Sven. Vetenskapsakad. Handl. 24 (1898) 1–39.
[52] K.L. Yu, X.J. Lee, H.C. Ong, W.-H. Chen, J.-S. Chang, C.-S. Lin, P.L. Show, T.C. Ling, Adsorptive removal of cationic methylene blue and anionic Congo red dyes using wet-torrefied microalgal biochar: equilibrium, kinetic and mechanism modeling, Environ. Pollut. 272 (2021) 115986, https://doi.org/10.1016/j.envpol.2020.115986.
[53] I. Langmuir, The adsorption of gases on plane surfaces of glass, mica and platinum, J. Am. Chem. Soc. 40 (1918) 1361–1403, https://doi.org/10.1021/ja02242a004.
[54] H.M.F. Freundlich, Over the adsorption in solution, J. Phys. Chem. 57 (1906) 1100–1107.
[55] C.A. Başar, Applicability of the various adsorption models of three dyes adsorption onto activated carbon prepared waste apricot, J. Hazard Mater. 135 (2006) 232–241, https://doi.org/10.1016/j.jhazmat.2005.11.055.

[56] M.I. Temkin, Kinetics of ammonia synthesis on promoted iron catalysts, Acta Physicochim. URSS 12 (1940) 327–356.
[57] A. Mudhoo, Unveiling new insights: revised Temkin adsorption isotherm parameters from fresh curve fits in adsorption studies, Chem. Eng. Sci. 311 (2025) 121585, https://doi.org/10.1016/j.ces.2025.121585.
[58] M.M. El-Masry, M.M. Arman, Cobalt, nickel and zinc spinel ferrites with high transmittance and UV-blocking for advanced optical applications, Sci. Rep. 15 (2025) 16636, https://doi.org/10.1038/s41598-025-99604-6.
[59] L.-F. Liao, C.-F. Lien, D.-L. Shieh, M.-T. Chen, J.-L. Lin, FTIR study of adsorption and photoassisted oxygen isotopic exchange of carbon monoxide, carbon dioxide, carbonate, and formate on TiO_2, J. Phys. Chem. B 106 (2022) 11240–11245, https://doi.org/10.1021/jp0211988.
[60] A. Lassoued, J.F. Li, Magnetic and photocatalytic properties of Ni-Co ferrites, Solid State Sci. 104 (2020) 106199, https://doi.org/10.1016/j.solidstatesciences.2020.106199.
[61] V.P. Senthil, J. Gajendiran, S. Gokul Raj, T. Shanmugavel, G. Ramesh Kumar, C. Parthasaradhi Reddy, Study of structural and magnetic properties of cobalt ferrite ($CoFe_2O_4$) nanostructures, Chem. Phys. Lett. 695 (2018) 19–23, https://doi.org/10.1016/j.cplett.2018.01.057.
[62] J. Zuo, B. Wang, J. Kang, P. Yan, J. Shen, S. Wang, D. Fu, X. Zhu, T. She, S. Zhao, Z. Chen, Activation of peroxymonosulfate by nanoscaled $NiFe_2O_4$ magnetic particles for the degradation of 2,4-dichlorophenoxyacetic acid in water: efficiency, mechanism and degradation pathways, Separ. Purif. Technol. 297 (2022) 121459, https://doi.org/10.1016/j.seppur.2022.121459.
[63] B. Aslibeiki, Magnetic interactions and hysteresis loops study of $Co/CoFe_2O_4$ nanoparticles, Ceram. Int. 42 (2016) 6413–6421, https://doi.org/10.1016/j.ceramint.2016.01.044.
[64] G. Bona, G. Bragaggia, M. Cantoni, B. Di Credico, S. Mostoni, G. Capitani, R. Scotti, S. Gross, R. Nisticò, Polyethylene glycol-assisted hydro-solvothermal growth of anisotropic magnetic iron oxides: the role of mixed environment conditions, Colloids Surf. A Physicochem. Eng. Asp. 702 (2024) 135117, https://doi.org/10.1016/j.colsurfa.2024.135117.
[65] Z. Danková, A. Mockovčiaková, S. Dolinská, Influence of ultrasound irradiation on cadmium cations adsorption by montmorillonite, Desalination Water Treat. 52 (2014) 5462–5469, https://doi.org/10.1080/19443994.2013.814006.
[66] V. Tobilko, L. Spasonova, I. Kovalchuk, B. Kornilovych, Y. Kholodko, Adsorption of uranium(VI) from aqueous solutions by amino-functionalized clay minerals, Colloid Interface Sci. 3 (2019) 41, https://doi.org/10.3390/colloids3010041.
[67] P. Erdem, A.A. Tağaç, P. Tashakkori, S.S. Bozkurt, M. Merdivan, Biopolymer-imidazolium based dicationic ionic liquid modified clay bionanocomposite coating for solid-phase microextraction of phthalate esters, Microchem. J. 170 (2021) 106648, https://doi.org/10.1016/j.microc.2021.106648.
[68] W. Sun, X. Zha, S. Lu, J. Liu, G. Sun, X. Huang, Y. Wang, Linker-induced hollow MOF embedded into arginine-modified montmorillonite for efficient urea removal: adsorption behavior and mechanism analysis, Separ. Purif. Technol. 352 (2023) 128213, https://doi.org/10.1016/j.seppur.2024.128213.
[69] Z. Qiao, Z. Liu, S. Zhang, Y. Yang, Y. Wu, L. Liu, Q. Liu, Purification of montmorillonite and the influence of the purification method on textural properties, Appl. Clay Sci. 187 (2020) 105491, https://doi.org/10.1016/j.clay.2020.105491.
[70] X. Li, Y.M. Wang, S.J. Wu, H.R. Wang, X.C. Liu, H.D. Sun, L. Fan, Effect of montmorillonite modification on resistance to thermal oxidation aging of asphalt binder, Case Stud. Constr. Mater. 16 (2022) e00971, https://doi.org/10.1016/j.cscm.2022.e00971.
[71] I. Fatimah, I. Yanti, H.K. Wijayanti, E.U. Nisa, S. Sagadevan, M. Tamyiz, R. Doong, Montmorillonite-supported $NiFe_2O_4$ as magnetically separable and reusable oxidation catalyst, Mater. Lett. 344 (2020) 134444, https://doi.org/10.1016/j.matlet.2023.134444.
[72] P.K. Saikia, P.P. Sarmah, B.J. Borah, L. Saikia, K. Saikiaa, D.K. Dutta, Stabilized Fe_3O_4 magnetic nanoparticles into nanopores of modified montmorillonite clay: a highly efficient catalyst for the Baeyer–Villiger oxidation under solvent free conditions, Green Chemistry 18 (2016) 2843–2850, https://doi.org/10.1039/C5GC02668G.
[73] B. Zeynizadeh, S. Rahmani, Immobilized copper-layered nickel ferrite on acid-activated montmorillonite, [($NiFe_2O_4$@Cu)(H^+-Mont)], as a superior magnetic nanocatalyst for the green synthesis of xanthene derivatives, RSC Adv. 9 (2019) 28038–28052, https://doi.org/10.1039/C9RA04320A.
[74] B. Zeynizadeh, S. Rahmani, Sulfonyl-bridged (copper-immobilized nickel ferrite) with activated montmorillonite, [($NiFe_2O_4$@Cu)SO_2(MMT)]: a new class of magnetically separable clay nanocomposite systems towards Hantzsch synthesis of coumarin-based 1,4-dihydropyridines, RSC Adv. 9 (2019) 8002–8015, https://doi.org/10.1039/C9RA00177H.
[75] A. Quesada, F. Rubio-Marcos, J.F. Marco, F.J. Mompean, M. Garcia-Hernandez, J. F. Fernandez, On the origin of remanence enhancement in exchange-uncoupled $CoFe_2O4$-based composites, Appl. Phys. Lett. 105 (2014) 202405, https://doi.org/10.1063/1.4902351.
[76] F. Barraqué, M.L. Montes, M.A. Fernández, R.C. Mercader, R.J. Candal, R. M. Torres-Sánchez, Synthesis and characterization of magnetic-montmorillonite and magnetic-organo-montmorillonite: surface sites involved on cobalt sorption, J. Magn. Magn Mater. 466 (2018) 376–384, https://doi.org/10.1016/j.jmmm.2018.07.052.
[77] A.M. Saleh, H.H. Mahdi, A.B. Alias, N.K.A. Hadi, D. Qarizada, A.H. Jawad, N. M. Saleh, Equilibrium and kinetic studies in adsorption of H_2S using coconut shell activated carbon xerogel: effect of mass adsorbent and temperature, Desalination Water Treat. 317 (2024) 100149, https://doi.org/10.1016/j.dwt.2024.100149.
[78] I. Herath, P. Kumarathilaka, M.I. Al-Wabel, A. Abduljabbar, M. Ahmad, A.R. A. Usman, M. Vithanage, Mechanistic modeling of glyphosate interaction with rice husk derived engineered biochar, Microporous Mesoporous Mater. 225 (2016) 280–288, https://doi.org/10.1016/j.micromeso.2016.01.017.
[79] C.S.T. Araújo, I.L.S. Almeida, H.C. Rezende, S.M.L.O. Marcionilio, J.J.L. Léon, T. N. de Matos, Elucidation of mechanism involved in adsorption of Pb(II) onto lobeira fruit (*Solanum lycocarpum*) using Langmuir, Freundlich and Temkin isotherms, Microchem. J. 137 (2018) 348–354, https://doi.org/10.1016/j.microc.2017.11.009.
[80] R. Ramadan, N. Shehata, Adsorptive removal of methylene blue onto MFe_2O_4: kinetics and isotherm modeling, Desalination and Water Treatment 227 (2021) 370–383, https://doi.org/10.5004/dwt.2021.27248.
[81] H. Gomaa, E.M.A. El-Monaem, A.S. Eltaweii, A.M. Omer, Efficient removal of noxious methylene blue and crystal violet dyes at neutral conditions by reusable montmorillonite/$NiFe_2O_4$@amine-functionalized chitosan composite, Sci. Rep. 12 (2022) 12, https://doi.org/10.1038/s41598-022-19570-1.
[82] H. Ighnih, R. Haounati, H. Ouachtak, A. Regti, B. El Ibrahimi, N. Hafid, A. Jada, M. L. Taha, A.A. Addi, Efficient removal of hazardous dye from aqueous solutions using magnetic kaolinite nanocomposite: experimental and Monte Carlo simulation studies, Inorg. Chem. Commun. 153 (2023) 110886, https://doi.org/10.1016/j.inoche.2023.110886.
[83] F. Fei, Z. Gao, H. Wu, W. Wurendaodi, S. Zhao, S. Asuha, Facile solid-state synthesis of Fe_3O_4/kaolinite nanocomposites for enhanced dye adsorption, J. Solid State Chem. 291 (2020) 121655, https://doi.org/10.1016/j.jssc.2020.121655.
[84] M.K. Goswami, A. Srivastava, R.K. Dohare, A.K. Tiwari, A. Srivastav, Recent advances in conducting polymer-based magnetic nanosorbents for dyes and heavy metal removal: fabrication, applications, and perspective, Environ. Sci. Pollut. Control Ser. 30 (2023) 73031–73060, https://doi.org/10.1007/s11356-023-27458-4.